
Curvature is Key: Sub-Sampled Loss Surfaces and the Implications for Large Batch Training

Diego Granzio^{*}

Machine Learning Research Group
Oxford
United Kingdom
diego@robots.ox.ac.uk

Abstract

We study the effect of mini-batching on the loss landscape of deep neural networks using spiked, field-dependent random matrix theory. We show that the magnitude of the extremal values of the batch Hessian are larger than those of the empirical Hessian. Our framework yields an analytical expression for the maximal SGD learning rate as a function of batch size, informing practical optimisation schemes. We use this framework to demonstrate that accepted and empirically-proven schemes for adapting the learning rate emerge as special cases of our more general framework. For stochastic second order methods and adaptive methods, we derive that the minimal damping coefficient is proportional to the ratio of the learning rate to batch size. For adaptive methods, we show that for the typical setup of small learning rate and small damping, square root learning rate scalings with increasing batch-size should be employed. We validate our claims on the VGG/WideResNet architectures on the CIFAR-100 and ImageNet datasets.

1 Introduction

Deep Learning has taken computer vision and natural language processing tasks by storm. The observation that different critical points post similar test set performance, has spawned an explosion of theoretical [14, 15, 58] and empirical interest [21, 42, 62, 63, 71], in their loss surfaces, typically through study of the eigenspectrum of the Hessian. Scalar metrics of the Hessian, such as the trace/spectral, have been related to generalisation [39, 42]. Under a Bayesian [45] and minimum description length framework [31], flatter minima generalize better than sharp minima. Theoretical work on the Hessian of neural networks, has shown that all local minima are close to the global [14] and that critical points of high index have high loss values [58]. Second order optimisation methods [8], use the Hessian (or semi positive definite approximations thereof, such as the Fisher information matrix). They more efficiently navigate along narrow and sharp valleys, making significantly more progress per iteration [46, 50, 49, 18] than first order methods.

A crucial part of practical deep learning is the concept of sub-sampling or mini-batching. Instead of using the entire dataset of size N to evaluate the loss, gradient or Hessian at each training iteration, only a small randomly chosen subset of size $B \ll N$ is used. This allows faster progress and lessens the computational burden tremendously. However, despite its widespread use in optimisation, the precise characterisation of the effect of mini-batching on the loss landscape and implications thereof, have not been thoroughly investigated. In this paper we show that,

^{*}The first author would like to explicitly acknowledge the help of Xingchen Wan, in implementing the generalised Gauss Newton vector product and KFAC in Pytorch, extensive text scrutiny and figure proofing.

- Under assumptions consistent with the optimisation paradigm, the Hessian noise due to mini-batching can be modelled as a random matrix.
- When well separated from the noise matrix (which we define in Section 2.1), the extremal eigenvalues of the batch Hessian are given by the extremal eigenvalues of the full Hessian plus a term proportional to the ratio of the *Hessian variance* to the batch size. We verify this empirically for the VGG-16 [65] on the CIFAR-100 dataset.
- This result predicts initial perfect scaling, diminishing returns and stagnation when increasing the batch size of stochastic gradient descent training [22, 64]. This result is crucial for understanding how to alter learning rate schedules when exploiting large batch training and data-parallelism, or when using limited GPU capacity for small or mobile devices.
- The minimum damping term of stochastic second order methods ², is inversely proportional to the batch size. For adaptive gradient methods where the damping parameter is fixed to a small value, such as the Adam default settings, we derive and verify the efficacy of a square root learning rate scaling rule with batch size.

Motivation: For samples drawn independently from the training set, the stochastic gradient $\mathbf{g}_i(\mathbf{w}) \in \mathbb{R}^{P \times 1}$ in expectation is equal to the empirical gradient $\mathbb{E}(\mathbf{g}_i(\mathbf{w})) = \mathbf{g}(\mathbf{w})$ [9, 52]. However for the sample inverse Hessian $\mathbf{H}_i^{-1}(\mathbf{w}) \in \mathbb{R}^{P \times P}$. $\mathbb{E}(\mathbf{H}_i^{-1}(\mathbf{w})) \neq \mathbf{H}^{-1}(\mathbf{w})$, as the inverse is not a linear operator. By the spectral theorem, every Hermitian matrix, can be represented by its spectrum $\mathbf{H}(\mathbf{w}) = \sum_i^P \lambda_i \phi_i \phi_i^T$ and hence the spectrum of $\mathbf{H}_i(\mathbf{w})$ differs from that of $\mathbf{H}(\mathbf{w})$. Mini-batching is prevalent in all [49, 18] deep learning second order optimisation methods. Proofs of convergence for this class of methods explicitly require similarity between the sub-sampled and full dataset Hessian spectrum [61]. Hence, understanding the spectral perturbations due to mini-batching is of great importance for second order methods. For gradient methods on convex functions, the convergence rate, optimal and maximal learning rates are functions of the Lipschitz constant [52], which is the infimum of the eigenvalues of the Hessian in the weight manifold. Hence understanding the largest eigenvalue perturbation due to mini-batching also has direct implications for their stability and convergence.

Related Work: To the best of our knowledge no prior work has theoretically or empirically compared the Hessian of the full dataset and that of a mini-batch and the consequences thereof. Hence the problem statement, theory and focus of this work are novel. Previous works focusing on the loss landscape structure as a function of loss value [14, 58], assume normality and independence of the inputs and weights ³. Removing these assumptions is considered a major open problem [15], addressed in the deep linear case with squared loss [38]. Furthermore, the spectra are not compatible with outliers, extensively observed in practice [62, 63, 21, 54]. We address both concerns, by considering a field dependence structure [25], non identical element variances and modeling the outliers explicitly as low rank perturbations [3]. This may be of more general use to the community outside of our applications. Our framework, prescribes a linear scaling rule up until a threshold for stochastic gradient descent. [41, 26] also prescribe a linear scaling of learning rate with batch size, however it is justified under the unrealistic assumption that the gradient is the same at all points in weight space. [35] show linear parallelisation and then thresholding for least squares linear regression, assuming strong convexity. Our results hold for more general losses and does not assume strong convexity. Other work which considers the effect of batch sizes on learning rate choices and various optimisation algorithms, considers a constant as opposed to evolving Hessian and relies on assumptions of co-diagonalizability of the Hessian and Covariance of the gradients [73], which is not necessary in our framework. We derive an inverse relationship between the damping co-efficient of stochastic second order methods and batch size, which is to our knowledge novel. For adaptive or stochastic second order methods using small damping and small learning rates, our theory prescribes a square root scaling procedure. [32] also prescribes a square root scaling based on the co-variance of the gradients, for SGD but not adaptive methods.

²often grid-searched as an extra hyper-parameter [18] or adjusted during training [48]

³and often even more assumptions, such as i.i.d Hessian elements and free addition [58] which means that we can simply add the spectra of two matrices

2 Random matrix theoretic approach to the Batch Hessian

For an input, output pair $[\mathbf{x}, \mathbf{y}] \in [\mathbb{R}^{d_x}, \mathbb{R}^{d_y}]$ and a given prediction function $h(\cdot; \cdot) : \mathbb{R}^{d_x} \times \mathbb{R}^P \rightarrow \mathbb{R}^{d_y}$, we consider the family of prediction functions parameterised by a weight vector \mathbf{w} , i.e., $\mathcal{H} := \{h(\cdot; \mathbf{w}) : \mathbf{w} \in \mathbb{R}^P\}$ with a given loss function $\ell(h(\mathbf{x}; \mathbf{w}), \mathbf{y}) : \mathbb{R}^{d_y} \times \mathbb{R}^{d_y} \rightarrow \mathbb{R}$. In conjunction with statistical learning theory terminology, we denote the loss over our data generating distribution $\psi(\mathbf{x}, \mathbf{y})$, as the *true risk*. $R_{true}(\mathbf{w}) = \int \ell(h(\mathbf{x}; \mathbf{w}), \mathbf{y}) d\psi(\mathbf{x}, \mathbf{y})$, with corresponding gradient $\mathbf{g}_{true}(\mathbf{w}) = \nabla R_{true}(\mathbf{w})$ and Hessian $\mathbf{H}_{true}(\mathbf{w}) = \nabla \nabla R_{true}(\mathbf{w})$. We discuss the true Hessian in Appendix E. Given a dataset of size N , we only have access to the *empirical risk* $R_{emp}(\mathbf{w}) = \sum_{i=1}^N \ell(h(\mathbf{x}_i; \mathbf{w}), \mathbf{y}_i)/N$, empirical gradient $\mathbf{g}_{emp}(\mathbf{w}) = \nabla R_{emp}(\mathbf{w})$ and empirical Hessian $\mathbf{H}_{emp}(\mathbf{w}) = \nabla \nabla R_{emp}(\mathbf{w})$. To further reduce computation cost, often only the batch risk $R_{batch}(\mathbf{w}) = \sum_{i=1}^B \ell(h(\mathbf{x}_i; \mathbf{w}), \mathbf{y}_i)/B$, where $B \ll N$ and the gradients $\mathbf{g}_{batch}(\mathbf{w})$, Hessians $\mathbf{H}_{batch}(\mathbf{w})$ thereof are accessed. The Hessian describes the curvature at that point in weight space \mathbf{w} and hence the risk surface can be studied through the Hessian.

2.1 Properties of the noise matrix

We write the stochastic batch Hessian as the deterministic empirical Hessian plus the noise matrix. $\mathbf{H}_{batch}(\mathbf{w}) = \mathbf{H}_{emp}(\mathbf{w}) + \epsilon(\mathbf{w})$.⁴ Rewriting the noise matrix as $\epsilon(\mathbf{w}) \equiv \mathbf{H}_{batch}(\mathbf{w}) - \mathbf{H}_{emp}(\mathbf{w})$ and assuming the dataset to be drawn independently from the data generating distribution, we can infer

$$\begin{aligned} \epsilon(\mathbf{w}) &= \left(\frac{1}{B} - \frac{1}{N} \right) \sum_j^B \nabla \nabla \ell(\mathbf{x}_j, \mathbf{w}; \mathbf{y}_j) - \frac{1}{N} \sum_{i \neq j}^N \nabla \nabla \ell(\mathbf{x}_i, \mathbf{w}; \mathbf{y}_i) \\ \therefore \mathbb{E}(\epsilon(\mathbf{w})_{j,k}) &= 0, \quad \mathbb{E}(\epsilon(\mathbf{w})_{j,k})^2 = \left(\frac{1}{B} - \frac{1}{N} \right) \text{Var}[\nabla \nabla \ell(\mathbf{x}, \mathbf{w}; \mathbf{y})_{j,k}] \end{aligned} \quad (1)$$

Where the expectation is taken with respect to the data generating distribution $\psi(\mathbf{x}, \mathbf{y})$. In order for the variance in equation 1 to exist, the elements of $\nabla \nabla \ell(\mathbf{w}, \mathbf{w}; \mathbf{y})$ must obey sufficient moment conditions. This can either be assumed as a technical condition, or alternatively derived under the more familiar condition of L -Lipschitz continuity, as shown with the following lemma.

Lemma 1. *For an L -Lipschitz-continuous-gradient and almost everywhere twice differentiable loss function $\ell(h(\mathbf{x}; \mathbf{w}), \mathbf{y})$, the True Hessian elements $\mathbf{H}_{j,k} \equiv [\int \ell(\nabla \nabla h(\mathbf{x}; \mathbf{w}), \mathbf{y}) d\psi(\mathbf{x}, \mathbf{y})]_{j,k}$ are strictly bounded in the range $-\sqrt{PL} \leq \mathbf{H}_{j,k} \leq \sqrt{PL}$.*

Proof. By the fundamental theorem of calculus and the definition of Lipschitz continuity $\lambda_{max} \leq L$

$$\begin{aligned} \text{Tr}(\mathbf{H}^2) &= \sum_{j,k=1}^P \mathbf{H}_{j,k}^2 = \mathbf{H}_{j=j',k=k'}^2 + \sum_{j \neq j', k \neq k'}^P \mathbf{H}_{j,k}^2 = \sum_{i=1}^P \lambda_i^2 \\ \therefore \mathbf{H}_{j=j',k=k'}^2 &\leq \sum_{i=1}^P \lambda_i^2 \leq PL^2 \quad \therefore -\sqrt{PL} \leq \mathbf{H}_{j=j',k=k'} \leq \sqrt{PL} \end{aligned} \quad (2)$$

□

Remark. As the domain of the Hessian elements under the data generating distribution are bounded, the moments of equation 1 are bounded and hence the variance exists. We can even go a step further

Lemma 2. *For independent samples drawn from the data generating distribution and an L -Lipshitz loss ℓ the difference between the empirical Hessian and Batch Hessian converges element-wise to a zero mean, normal random variable with variance $\propto \frac{1}{B} - \frac{1}{N}$ for large B, N .*

Proof. By Lemma 1, the Hessian elements are bounded, hence the moments are bounded and using independence of samples and the central limit theorem [66], $(\frac{1}{B} - \frac{1}{N})^{-1/2} [\nabla \nabla R_{true}(\mathbf{w}) - \nabla \nabla R_{emp}(\mathbf{w})]_{jk} \xrightarrow{a.s} \mathcal{N}(0, \sigma_{jk}^2)$.

⁴Note that although we could write $\mathbf{H}_{emp}(\mathbf{w}) = \mathbf{H}_{batch}(\mathbf{w}) - \epsilon(\mathbf{w})$, this treatment is not symmetric as $\mathbf{H}_{batch}(\mathbf{w})$ is dependent on $\epsilon(\mathbf{w})$, whereas $\mathbf{H}_{emp}(\mathbf{w})$ is not.

□

To derive analytic results, we employ the Kolmogorov limit [11], where $P, N \rightarrow \infty$ but $P/N = q > 0$ and to account for dependence beyond the symmetry of the noise matrix elements, we introduce the σ -algebras, and Lindeberg's ratio $L_n(\tau)$, which for any $\tau > 0$

$$\begin{aligned} \mathfrak{F}^{(i,j)} &:= \sigma\{\mathbf{H}_{kl} : 1 \leq k \leq l \leq P, (k, l) \neq (i, j)\}, q \leq i \leq j \leq P \\ L_P(\tau) &:= \frac{1}{P^2} \sum_{i,j=1}^P \mathbb{E}|\mathbf{H}_{i,j}|^2 \mathbb{1}(|\mathbf{H}_{i,j}| \geq \tau\sqrt{P}) \end{aligned} \quad (3)$$

Theorem 1. *Under the conditions of Lemmas 1 and 2 along with the following technical conditions that in the limit $n \rightarrow \infty$, the limiting spectra density of $\epsilon(\mathbf{w})$ is given by Wigners semi-circle law*

- i) $\frac{1}{P^2} \sum_{i,j=1}^P \mathbb{E}|\mathbb{E}(\mathbf{H}_{i,j}^2 | \mathfrak{F}^{i,j}) - \sigma_{i,j}^2| \rightarrow 0$,
- ii) $L_P(\tau) \rightarrow 0$ for any $\tau > 0$,
- iii) $\frac{1}{P} \sum_i |\frac{1}{P} \sum_{j=1}^P \sigma_{i,j}^2 - \sigma_\epsilon^2| \rightarrow 0$
- iv) $\max_{1 \leq i \leq P} \frac{1}{P} \sum_{j=1}^P \sigma_{i,j}^2 \leq C$

Proof Sketch. By Lemma 1 the Lindenberg condition, i.e condition holds *ii*). By Lemma 2 we also have $\mathbb{E}(\mathbf{H}_{i,j} | \mathfrak{F}^{i,j}) = 0$ and the rest of the proof is given by Gotze et al [25]. [25] use the condition $\frac{1}{P} \sum_i |\frac{1}{P} \sum_{j=1}^P \sigma_{i,j}^2 - 1| \rightarrow 0$, however this simply introduces a simple scaling factor. □

Theorem 2. *under the assumption \mathbf{H}_{emp} is of low rank $r \ll P$, The extremal eigenvalues $[\lambda'_1, \lambda'_P]$ of the matrix sum $\mathbf{H}_{batch}(\mathbf{w}) = \mathbf{H}_{emp}(\mathbf{w}) + \epsilon(\mathbf{w})$, where $\lambda'_1 \geq \lambda'_2 \dots \geq \lambda'_P$, where $\mathbf{H}_{emp}(\mathbf{w})$ has extremal eigenvalues $[\lambda_1, \lambda_P]$, given by*

$$\lambda'_1 = \begin{cases} \lambda_1 + \frac{P}{\mathfrak{b}} \frac{\sigma_\epsilon^2}{\lambda_1}, & \text{if } \lambda_1 > \sqrt{\frac{P}{\mathfrak{b}}} \sigma_\epsilon \\ 2\sqrt{\frac{P}{\mathfrak{b}}} \sigma_\epsilon, & \text{otherwise} \end{cases}, \lambda'_P = \begin{cases} \lambda_P + \frac{P}{\mathfrak{b}} \frac{\sigma_\epsilon^2}{\lambda_P}, & \text{if } \lambda_P < -\sqrt{\frac{P}{\mathfrak{b}}} \sigma_\epsilon \\ -2\sqrt{\frac{P}{\mathfrak{b}}} \sigma_\epsilon, & \text{otherwise} \end{cases}. \quad (4)$$

Where $\mathfrak{b} = B/(1 - B/N)$ and B is the batch-size. The factor \mathfrak{b} has appeared before [37, 35]

Proof Sketch. Combining Theorem 1 with known results of the spiked Wigner model [3] and the necessary scaling factors from Lemmas 1 and 2 we arrive at the result. □

Remark. Although for clarity we only focus on the extremal eigenvalues, the proof as shown in Appendix A holds for all outlier eigenvalues which are outside the spectrum of the noise matrix.

Remark. The assumption that either \mathbf{H}_{emp} or $\epsilon(\mathbf{w})$ are low rank is necessary to use perturbation theory in the proof. This condition could be relaxed if a substantial part of the eigenspectrum of \mathbf{H}_{emp} were considered to be mutually free with that of $\epsilon(\mathbf{w})$ [11]. In Appendix B we derive a bound on the rank of a feed-forward network, which we show to be small for large networks and provide extensive experimental evidence that the full Hessian is in fact low rank.

Remark. In the special case that $\epsilon(\mathbf{w})_{i,j}$ are i.i.d Gaussian, the noise matrix is the Gaussian Orthogonal Ensemble, proposed as the spectral density of the Hessian by Choromanska et al. [14]. In this case, Theorem 2 can be proved more succinctly, which we detail in full in the Appendix A.

We illustrate the result in Figure 1. If the largest Hessian eigenvalue is well separated from the noise matrix, as shown in Figure 1a, then increasing the batch size, which reduces the spectral width of the noise matrix, will have an approximately linear effect in reducing the spectral norm. This will hold up until a threshold, shown in Figure 1b, after which the spectral norm no longer appreciably changes in size. In the case that the spectral norm of the full dataset Hessian is smaller than that of the noise matrix, shown in Figure 1c, the largest eigenvalue of the batch Hessian, which is given by the noise matrix, will reduce as the square root of the batch size, again up until a critical level shown in Figure 1d.

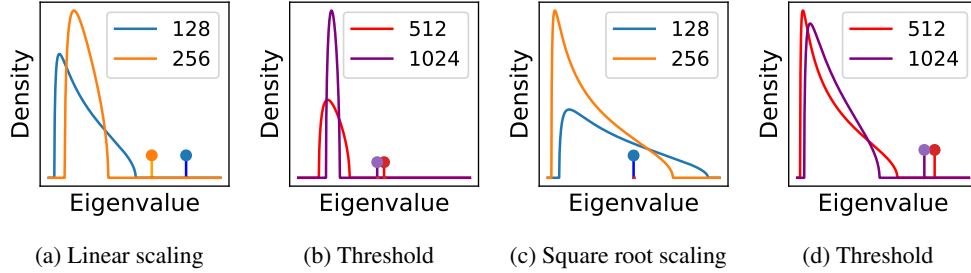


Figure 1: Stylised Hessian spectral density plot with varying batch size. Continuous region corresponding to the noise matrix induced by mini-batching and the largest eigenvalue of the full Hessian shown as a peak. Scaling refers to how the largest eigenvalue decreases as the batch size is increased. Threshold denotes no major change.

3 Experimental validation

For simplicity, we do not analyse the added dependence between curvature and the samples due to batch normalisation [34] and hence adopt a reference model VGG-16 [65] on the CIFAR-100 dataset which does not utilise batch normalisation. We show in Appendix H that many of our results also hold with batch-normalisation. We plot an example effect of the spectral broadening of the Hessian due to mini-batching, for a typical batch size of $B = 128$ in Figure 2. The magnitude of the extremal eigenvalues are significantly increased as are other outlier eigenvalues, such as the second largest. We estimate the mean of the continuous region (bulk) of the spectrum as where Ritz⁵ weight drops to below $1/P$. We see that the spectral width of this continuous region also increases.

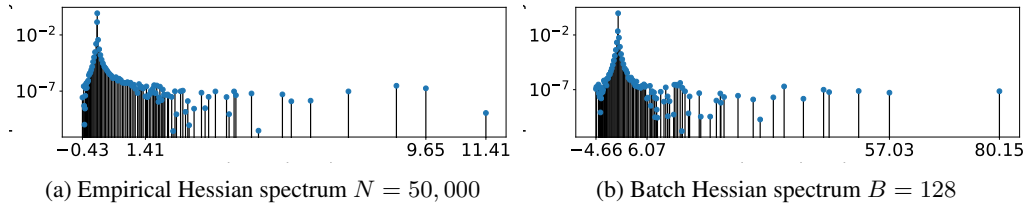


Figure 2: Spectral Density of the Hessian at epoch 200 , on a VGG-16 on the CIFAR-100 dataset

4 Extension to Fisher information and other positive definite matrices

In the case of Softmax regression, which is simply a 0 hidden layer neural network with cross entropy loss, by the diagonal dominance theorem [17], the Hessian is semi-positive definite and positive definite with the use of $L2$ regularisation. Hence an underlying noise matrix which contains negative eigenvalues is unsatisfactory and we extend our noise model to cover the positive semi definite case. Other common semi positive definite approximations to the Hessian in deep learning [47] include the Generalised Gauss Newton (GGN) [46, 50] and Fisher information [49, 59]. For some common activations and loss functions typical in deep learning, such as the cross entropy loss and sigmoid activation is equivalent to the Fisher information matrix [55]. The batch Hessian may be expressed in terms of the activation σ at the output of the final layer $f(\mathbf{x})$ using the chain rule as

$$\mathbf{H}_{batch}(\mathbf{w})_{ij} = \sum_{b=1}^B \left(\sum_{k=0}^{d_y} \sum_{l=0}^{d_y} \frac{\partial^2 \sigma}{\partial f_l(\mathbf{x}) \partial f_k(\mathbf{x})} (f(\mathbf{x})) \frac{\partial f_l(\mathbf{x})}{\partial x_j} \frac{\partial f_k(\mathbf{x})}{\partial x_i} + \sum_{k=0}^{d_y} \frac{\partial \sigma}{\partial x_j} (f(\mathbf{x})) \frac{\partial f_k(\mathbf{x})^2}{\partial x_j \partial x_i} \right) / B \quad (5)$$

The first term on the LHS of equation 5 is known as the GGN matrix. The rank of a product is the minimum rank of its products so the GGN upper bounded by the $B \times d_y$. Following [63] due to the

⁵this is the term used by approximate eigenvalue/eigenvector pairs by the Lanczos algorithm, as detailed in Appendix D

convexity of the loss ℓ with respect with the output $f(\mathbf{x})$ we rewrite the GGN per sample as

$$\sum_{k,l=0}^{d_y} \sqrt{\frac{\partial \sigma^2}{\partial f_l(\mathbf{x}) \partial f_k(\mathbf{x})}(f(\mathbf{x}))} \frac{\partial f_l(\mathbf{x})}{\partial x_j} \times \sqrt{\frac{\partial \sigma^2}{\partial f_l(\mathbf{x}) \partial f_k(\mathbf{x})}(f(\mathbf{x}))} \frac{\partial f_k(\mathbf{x})}{\partial x_i} = \mathbf{J}_* \mathbf{J}_*^T \quad (6)$$

where \mathbf{J}_* is the Jacobian transformed in order to retain a similarity for the GGN in the case of the squared loss function [58], under which it has the form $\mathbf{G}(\mathbf{w}) = \mathbf{J} \mathbf{J}^T$. There are many potential candidate noise models, such as the free multiplicative and information plus noise [10, 30], typically for equations of the form in equation 6, we would write $\mathbf{J}_{*batch} = \mathbf{J}_{*true} \epsilon$ and hence $\mathbf{J}_{*batch} \mathbf{J}_{*batch}^T = \mathbf{J}_{*true} \epsilon \epsilon^T \mathbf{J}_{*true}$ [11]. The corresponding analysis, gives a very similar result to Theorem 2. So the key take away is that *Independent of the exact limiting spectral density of the noise matrix, we can consider the extremal eigenvalues of the True Hessian or generalised Gauss Newton to be a low rank perturbation of that noise matrix.*

Since we are unable to find a reference that adequately derives or states the Stieltjes transform of the generalised non-unit variance Marcenko-Pastur density, we derive the result in full ourselves here. This derivation closely follows [19], but generalises the result. Note that Feier [19] use a different convention for the Stiltjes transform

$$S_P(z) = \int_{\mathbb{R}} \frac{1}{x-z} d\mu_P = \frac{1}{P} \text{Tr}(\mathbf{M}_n / \sqrt{P} - zI)^{-1} \quad (7)$$

We consider a series of matrices

$$\mathbf{X}_N = \left(r_i^s / \sqrt{P} \right)_{1 \leq i \leq P, 2 \leq j \leq N} \quad (8)$$

where the entries r_i^s are 0 mean and variance σ^2 The Wishart matrix $\mathbf{W}_P = \mathbf{X}_P \mathbf{X}_P^T$ which has an (i, j) entry $\frac{1}{N} \sum_{s=1}^N r_i^s r_j^s$. Clearly, \mathbf{W}_P can be written as the sum of rank-1 contributions $\mathbf{W}_P^s = (r_i^s r_j^s)_{1 \leq i, j \leq P}$. Now as each element is of mean 0 and variance σ^2 , the expectation of the sum of the elements squared is given by $P^2 \sigma^4 / T^2 = \text{Tr}([\mathbf{W}_P^s]^2) = \lambda^2$ and hence the one eigenvalue is given by $\lambda = \frac{P}{T} \sigma^2 = \beta \sigma^2$. For large P , by the weak law of large numbers, this is also true for a single realisation of \mathbf{W}_P^s . By the strong law of large numbers the column vectors $\mathbf{r}^s = [r_1^s \dots r_P^s]^T$ and $\mathbf{r}^{s'}$ are almost surely orthogonal as $P \rightarrow \infty$ and hence the matrices \mathbf{W}_P^s are asymptotically free

The Stiltjes transform $S(z)$ of \mathbf{W}_P^s

$$\frac{1}{P} \text{Tr}(\mathbf{W}_P^s - zI)^{-1} = -\frac{1}{P} \sum_{k=0}^{\infty} \frac{\text{Tr}(\mathbf{W}_P^s)^k}{z^{k+1}} = -\frac{1}{P} \left(\frac{P-1}{z} + \frac{1}{z - \beta \sigma^2} \right) \quad (9)$$

Solving the quadratic for z , completing the square, dropping low order terms in P and noting by the definition of the Stiltjes transform that for large $|z| \sim -\frac{1}{z}$

$$\begin{aligned} z &= \frac{P(s\beta\sigma^2 - 1) \pm \sqrt{P^2(s\beta\sigma^2 - 1)^2 + 4Ps(P-1)\beta\sigma^2}}{2Ps} \\ z &= \frac{P(s\beta\sigma^2 - 1) \pm \sqrt{P^2(s\beta\sigma^2 + 1)^2 - 4Ps\beta\sigma^2}}{2Ps} \\ z &\approx \frac{P(s\beta\sigma^2 - 1) - P(s\beta\sigma^2 + 1) - \frac{2Ps\beta\sigma^2}{s\beta\sigma^2 + 1}}{2Ps} = -\frac{1}{s} + \frac{\beta\sigma^2}{P(s\beta\sigma^2 + 1)} \end{aligned} \quad (10)$$

And hence as the \mathbf{W}_P is the free convolution of the random matrices \mathbf{W}_P^s we simply multiply the \mathcal{R} transform of each matrix by N and as $\beta = P/N$

$$\begin{aligned} \mathcal{R}_{\mathbf{W}_P}(s) &= N \times \left(z - \frac{1}{s} \right) = \frac{N\beta\sigma^2}{P(s\beta\sigma^2 + 1)} = \frac{\sigma^2}{(s\beta\sigma^2 + 1)} \\ \mathcal{B}_{\mathbf{W}_P}(s) &= z = -\frac{1}{s} + \frac{\sigma^2}{(s\beta\sigma^2 + 1)} \end{aligned} \quad (11)$$

and hence

$$S_{\mathbf{W}_P} = \frac{-(z + \sigma^2(1 - \beta)) + \sqrt{(z + \sigma^2(1 - \beta))^2 - 4\beta\sigma^2 z}}{2\beta\sigma^2 z} \quad (12)$$

From here, using the definition of the Stiltjes transform and the relationship to the spectral density, $\text{Im}_{y \rightarrow 0}(\mathcal{S}\mathbf{W}_P(x + iy))/2\pi i$

we have the celebrated generalised Marcenko-pastur result.

$$\rho(y) = \frac{\sqrt{4\beta\sigma^2 y - (y + \sigma^2(1 - \beta))^2}}{2\beta\sigma^2 y} \quad (13)$$

Noting that the Stiltjes transform from Feier [19] is reversed in the convention of the sign [11], we take $z \rightarrow -z$. Now we apply for $\mathcal{T}(z) = z\mathcal{S}(z) - 1$ transform and the result from Benaych-Georges and Nadakuditi [3], i.e $\lambda'_i = \mathcal{T}(\frac{1}{\lambda_i})$, where the dash denotes the noisy transform.

$$\mathcal{T}(z) = \frac{z - \sigma^2(1 + \beta) - \sqrt{(z + \sigma^2(1 - \beta))^2 - 4\beta\sigma^2 z}}{2\beta\sigma^2} \quad (14)$$

Following through the algebra, with some simple cancellations, we arrive at a qualitatively similar result to Theorem 2.

Theorem 3. *The extremal eigenvalue λ'_1 of the matrix \mathbf{G}_{batch} , where \mathbf{G}_{emp} has extremal eigenvalue λ_1 , is given by*

$$\lambda'_i = \left\{ \begin{array}{ll} \frac{P\sigma^2}{b} (1 + \frac{\beta}{\lambda_i})(1 + \lambda_i), & \text{if } \lambda_i > \sigma\sqrt{\frac{P}{b}} \\ \sigma^2 \frac{P}{b}, & \text{otherwise} \end{array} \right\}. \quad (15)$$

Proof Sketch. Combine the multiplicative perturbation results [3], with the extension of the Marcenko-Pastur law for dependent entries [53] \square

Remark. We note that in the limit of $\sigma^2 \rightarrow 1$, ignoring P, b by folding them into σ , we have the same results as in [3], where they simply take $\theta = \theta - 1$. One point to note is that as the noise is multiplicative, a zero noise matrix will ofcourse give all eigenvalues zero. To avoid this we could consider the matrix plus noise model were our matrix is now the Marcenko Pastur.

We plot an example of the generalised Gauss Newton, which for cross entropy loss and softmax activation is equal to the Fisher [55] in Figure 3. We observe identical behaviour of bulk and outlier broadening.

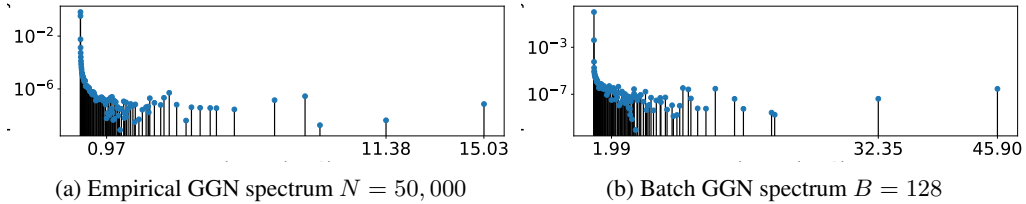


Figure 3: Spectral Density of the Generalised Gauss Newton (GGN) at epoch 25, on a VGG-16 on the CIFAR-100 dataset

We estimate the variance of the Hessian or GGN using stochastic trace estimation [33, 27] in Algorithm 1, from which the variance per element can be inferred. We plot the evolution of the Hessian/GGN variance throughout an SGD training cycle in Figure 4. This Figure implies that we expect the batch Hessian extremal eigenvalues to diverge from those of the empirical Hessian during training. To test this hypothesis we run both the SGD and KFAC [49] on the VGG-16 using CIFAR-100 and track the Hessian variance and full Hessian and the average of 10, $B = 128$ batch Hessian extremal eigenvalues and plot the results in Figure 5. The batch Hessian extremal eigenvalues have a large variance. This is to be expected as our results are in the limit $P, B \rightarrow \infty$ and corrections for finite B scale as $B^{-1/4}$ for matrices with finite 4th moments [1] which is $\approx 30\%$ for $B = 128$. Both the results from the additive noise process and multiplicative noise process give results within 1 standard deviation and follow the increase in variance of the Hessian in Figure 4. The multiplicative noise process gives a better fit. Recent work shows the Hessian outliers to be attributable to the GGN component of the spectrum [54]. Hence a positive semi definite noise process tailored for the GGN, would be expected to better estimate the outlier perturbations due to mini-batching, which we observe.

Algorithm 1 Calculate Hessian Variance

```
1: Input: Sample Hessian  $\mathbf{H}_i \in \mathbb{R}^{P \times P}$ 
2: Output: Hessian Variance  $\sigma^2$ 
3:  $\mathbf{v} \in \mathbb{R}^{1 \times P} \sim \mathcal{N}(\mathbf{0}, \mathbf{I})$ 
4:  $\mathbf{v} \leftarrow \mathbf{v} / \|\mathbf{v}\|$ 
5: Initialise  $\sigma^2 = 0, i = 0$ 
6: for  $i < P$  do
7:    $\sigma^2 \leftarrow \sigma^2 + \mathbf{v}^T \mathbf{H}_i^2 \mathbf{v}$ 
8:    $i \leftarrow i + 1$ 
9: end for
10:  $\sigma^2 \leftarrow \sigma^2 - [\mathbf{v}^T (1/N \sum_{j=1}^N \mathbf{H}_j) \mathbf{v}]^2$ 
```

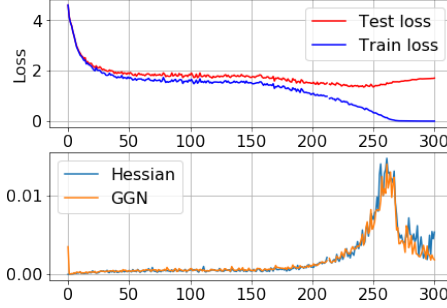


Figure 4: Loss/variance evolution throughout SGD training VGG-16 CIFAR-100

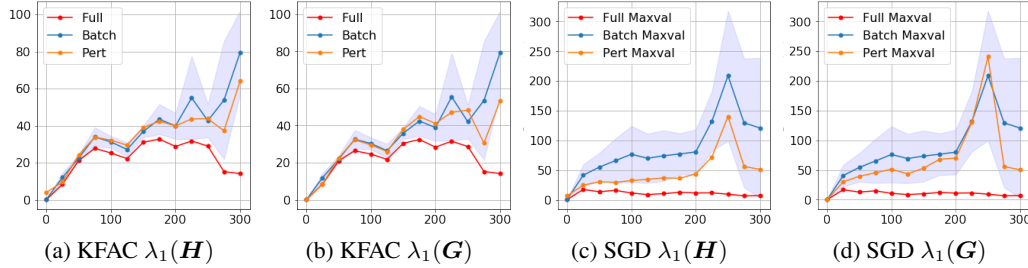


Figure 5: Evolution of the Variance σ and Maximal Eigenvalue λ_1 for both the Hessian \mathbf{H} and GGN \mathbf{G} , during SGD and KFAC training on the VGG-16 using the CIFAR-100 dataset. Full, Batch and Pert refer to the full, batch and the theoretically predicted Hessian eigenvalues respectively.

5 Application 1: SGD learning rates as a function of batch size

One key practical application of Section 2 for neural network training is its implications for learning rates as we alter the batch size. The loss to second order for a small step in the direction of the gradient is given by

$$\delta L(\mathbf{w} - \alpha \nabla L) = -\alpha \|\mathbf{g}(\mathbf{w})\|^2 \left(1 - \frac{\alpha \sum_i^P \lambda_i \|\phi_i \mathbf{g}(\mathbf{w})\|^2}{2} \right) \leq -\alpha \|\mathbf{g}(\mathbf{w})\|^2 \left(1 - \frac{\alpha \lambda_1}{2} \right) \quad (16)$$

and hence $\alpha < 2/\lambda_1$ to guarantee a decrease in loss. Where $\lambda_1(\mathbf{H}_{batch})$ and similarly all outlier eigenvalues of the batch Hessian are given by Theorem 2. A key term in equation 16 is the overlap between the eigenvectors and the stochastic gradient, shown to be large in practice [21, 29]. This indicates that the outlier broadening effect predicted by our framework (when there are well separated outliers⁶), i.e $\lambda_{i*} \approx \lambda_i + P\sigma^2/B\lambda_i$, is relevant to determining the maximal allowed learning rate. We observe outliers in all our experiments, as shown in Figures 2, 3, which is consistent with previous literature [21, 54]. Large learning rates have been shown to induce implicit regularisation [43]. In contrast, too small learning rates have been shown to lead to poor generalisation [36, 4]. Hence learning the largest stable learning rate is an important practical question for neural network training. For small batch sizes the maximal learning rate is proportional to the batch size. This holds until the first term in Theorem 2 is no longer negligible with the latter. To validate this empirically, we train the VGG-16 on CIFAR-100, finding the maximal learning rate at which the network trains for $B = 128$. We then increase/decrease the batch size by factors of 2, proportionally scaling the learning rate. We plot the results in Figure 6a. The validation accuracy remains stable for all batch size values, until a small drop for $B = 1024$, a larger drop still for $B = 2048$ and for $B = 4096$ we see no training. As shown in Appendix G, the accuracy curves are stable until the limiting batch size of size $B = 1$. Another theoretical prediction, is that if the Hessian variance increases during training (as observed in Figure 4), large learning rates which initially rapidly decrease the loss could become unstable later in training, which we observe in Figure 6b. To highlight the generality of this result, we include batch normalisation [34] and weight decay $\gamma = 0.0005$. In this case there is a greater range

⁶If there are no outliers, we expect the largest eigenvalue to decrease as the square root of the batch size.

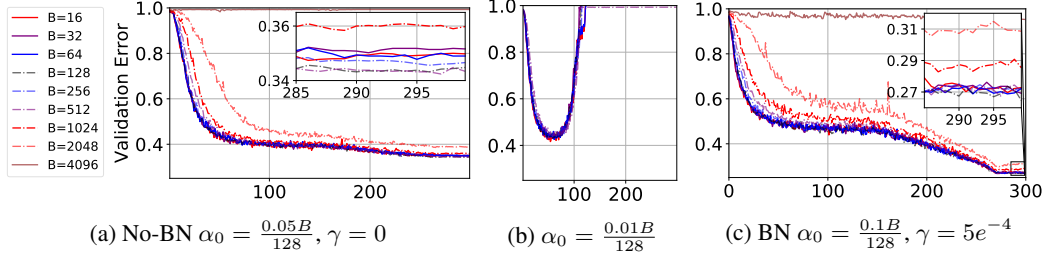


Figure 6: Validation error of the VGG-16, with and without batch normalisation (BN) on the CIFAR-100, with corresponding weight decay γ and initial learning rate α_0

of permissible learning rates, so we grid search the best learning rate as defined by the validation error for $B = 128$ and use our derived linear scaling rule, with the results shown in Figure 6c, where we observe a similar pattern. We repeat the experiment on the WideResNet- 28×10 [72] on both the CIFAR-100 and ImageNet 32×32 [16] datasets shown in Figure 7. Unlike the VGG without batch normalisation, where unstable trajectories diverge or with batch normalisation do not train. Highly unstable oscillatory WideResNet trajectories converge with learning rate reduction, however they never reach peak performance. The test performance is stable for a variety of learning rates with fixed learning rate to batch size ratio. Again confirming the validity of the linear scaling rate rule until a threshold. As shown in Appendix G, batch normalisation networks, which require the estimation of a variance parameter, degrade in quality below a batch size of 8 and do not train when $B = 1$. We do not experiment with ghost batch and group normalization [67, 32]. We also evaluate the difference between our predicted linear learning rate scaling and alternative schedules, such as the square root scaling

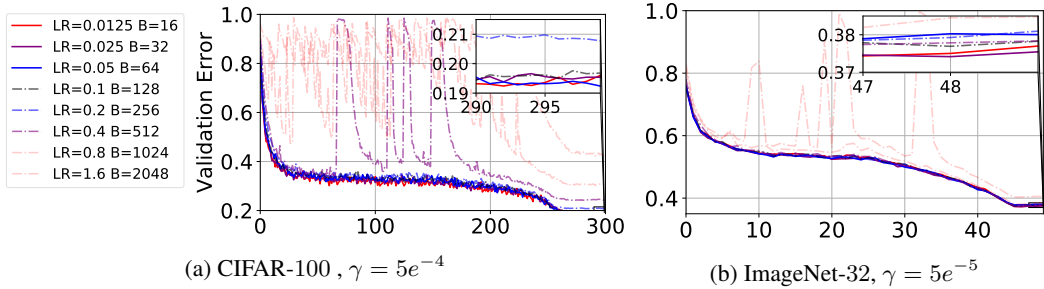


Figure 7: Validation error of the WideResNet- 28×10 on the CIFAR-100 and ImageNet32 dataset, with initial learning rate $\alpha_0 = \frac{0.1B}{128}$ and weight decay γ

6 Application 2: learning rates/damping for 2^{nd} order/adaptive optimisation

Damping: Second order methods minimise the quadratic around a small perturbation of the Loss $L(\mathbf{w} + \delta\mathbf{w})$ i.e $\delta\mathbf{w}^* = \arg \min_{\delta\mathbf{w}} \left(L(\mathbf{w}) + \nabla L(\mathbf{w})\delta\mathbf{w} + \frac{1}{2}\delta\mathbf{w}^T \mathbf{H}(\mathbf{w})\delta\mathbf{w} \right) = -\mathbf{H}^{-1}(\mathbf{w})\nabla L(\mathbf{w})$

Where in practice $\mathbf{H}^{-1} = \sum_i^P (\lambda_i + \delta)^{-1} \phi_i \phi_i^T$ and δ (the damping coefficient) keeps the optimizer within a trust region [50], limiting its ability to take overly large steps in locally flat directions. It is typically set at constant values and grid searched [18, 69]. Hence δ introduces partial adaptivity, at 0 we have a fully second order method and at $\delta \gg \lambda_{max}$ we resort to SGD with learning rate α_0/δ . Using our additive noise model from section 2, we can derive an analytic equation for the minimum damping required for a given batch size. The overlap between the batch extremal eigenvectors and their full dataset counterparts is given as (shown in Appendix A) $|\phi_i^T \hat{\phi}_i|^2 = 1 - P\sigma^2/b\lambda_i^2$. By considering the change in loss for a generic second order optimiser, writing $\mathbf{H}_{emp} = \sum_i \lambda_i \psi_i^T \psi$

and writing the noisy estimated eigenvalue/eigenvector from the optimiser as λ_i, ϕ_i , we have

$$L(\mathbf{w}_{k+1}) - L(\mathbf{w}) = \sum_i^P \frac{\alpha_0 |\phi_i^T \nabla L(\mathbf{w})|^2}{\lambda_i + \delta} \left(1 - \frac{\alpha_0}{2(\lambda_i + \delta)} \sum_{\mu} \lambda_{\mu} |\psi_{\mu}^T \phi_i|^2 \right) \therefore \delta > \frac{\alpha_0 P \sigma^2}{2b} \quad (17)$$

Where we assume δ to be sufficiently large. Hence the largest loss increase is due estimated flat directions having residual overlap with the sharpest direction of the loss. The total residual overlap is $P\sigma^2/b\lambda_i^2$ and for typical positive definite approximations [48, 69, 18], in the worst case, $\lambda_i \ll \delta$ in these directions, from which the result follows. To verify the validity of this relation, we run both the KFAC [49] and Adam [40] optimisers on the VGG-16 with no weight decay, with $\alpha = 1$, grid searching δ until we train to good accuracy⁷. The the batch size is increased/decreased by factors of 2 and the damping in inverse proportion. We display the validation errors for KFAC and Adam in Figures 8a and 8b respectively, where we note good agreement with theory.

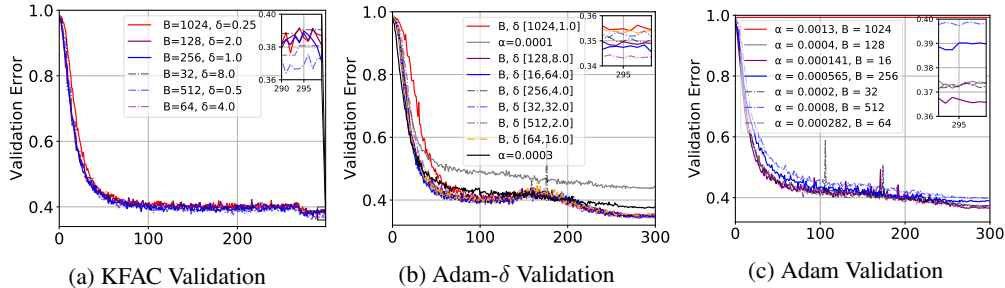


Figure 8: Error of the VGG-16 on the CIFAR-100 dataset for the KFAC and Adam optimisers. Adam- δ refers to Adam but with δ tuned as a function of batch size, as opposed to a default of 10^{-8}

Damping and Generalisation: For Adam $\delta = 10^{-8}$ is the default setting, trained with a low learning rate to compensate. We show the testing curves of typical learning rate values used [$1e^{-4}, 3e^{-4}$] to Figures 8b. Although not faster or better initially, such curves soon train better and generalise worse. We do not employ weight decay in this experiment, hence regularisation implementations [44] are not relevant. each optimization step is $-\sum_i^P (\lambda_i/\alpha_0 + \delta/\alpha_0)^{-1} \phi_i \phi_i^T \nabla L(\mathbf{w})$ and hence for fixed δ/α_0 , smaller α_0 takes smaller directions in the sharp loss directions, which seems to impact generalisation. Tuning the damping coefficient has been shown to improve generalisation in [13].

6.1 Square root learning rate scaling for adaptive optimisers with small damping

From equation 17, for small δ the greatest loss changes could result from large steps along flat directions. From Theorem 2 we expect the sharpness of some of these directions to grow inversely proportionally to the square root of the batch size. This implies that if our damping is small, we should scale the learning rate as the square root of batch size. We try this for the Adam optimiser with the default damping of 10^{-8} . We grid search the largest stable learning rate for a batch size of 128 and then increase/decrease the batch size by a factor of 2, scaling the learning rate proportional to the square root of the batch size change. We show the results in Figure 8c, which validates our hypothesis, whereas the linear prescription fails completely.

7 Conclusion

This paper shows under a spiked, field dependent random matrix theory framework that the extremal eigenvalues of the batch Hessian are larger than those of the empirical Hessian. The magnitude of the perturbation is inversely proportional to the batch size if there are well separated outliers in the Hessian spectrum and inversely proportional to the square root if not. The main implications of this work are that up until a threshold: 1) SGD learning rates should be scaled linearly with batch size. 2) Adam learning rates should be scaled with the square root of the batch size. 3) Damping in

⁷In the adam optimiser δ is given as ϵ and usually set to a default value of 10^{-8}

stochastic second order methods should be proportional to the ratio of learning rate to batch size. We also note empirically that taking larger steps in the sharp directions of the loss landscape seems to be related to improved generalisation. We validate our predictions and implications extensively on the VGG-16 network and CIFAR-100 dataset, with various hyper-parameter settings, including weight decay and batch-normalisation. For SGD, we further extend validate our prediction on the WideResNet 28×10 on the CIFAR-100 and ImageNet-32 datasets. Given that our analysis is neither dataset or architecture specific, we expect our results to hold generally outside of our experimental setup. This work can be used to better inform practitioners of how to adapt learning rate schedules for both small and large devices in a principled manner.

References

- [1] Zhi Dong Bai. Convergence rate of expected spectral distributions of large random matrices part i: Wigner matrices. In *Advances In Statistics*, pages 60–83. World Scientific, 2008.
- [2] Jinho Baik and Jack W Silverstein. Eigenvalues of large sample covariance matrices of spiked population models. *Journal of multivariate analysis*, 97(6):1382–1408, 2006.
- [3] Florent Benaych-Georges and Raj Rao Nadakuditi. The eigenvalues and eigenvectors of finite, low rank perturbations of large random matrices. *Advances in Mathematics*, 227(1):494–521, 2011.
- [4] Leonard Berrada, Andrew Zisserman, and M Pawan Kumar. Deep Frank-Wolfe for neural network optimization. *arXiv preprint arXiv:1811.07591*, 2018.
- [5] Rajendra Bhatia. *Matrix analysis*, volume 169. Springer Science & Business Media, 2013.
- [6] Alex Bloemendal, Antti Knowles, Horng-Tzer Yau, and Jun Yin. On the principal components of sample covariance matrices. *Probability theory and related fields*, 164(1-2):459–552, 2016.
- [7] Alex Bloemendal, Bálint Virág, et al. Limits of spiked random matrices ii. *The Annals of Probability*, 44(4):2726–2769, 2016.
- [8] Léon Bottou, Frank E Curtis, and Jorge Nocedal. Optimization methods for large-scale machine learning. *Siam Review*, 60(2):223–311, 2018.
- [9] Stephen P. Boyd and Lieven Vandenbergh. *Convex optimization*. Cambridge University Press, 2009.
- [10] Joël Bun, Romain Allez, Jean-Philippe Bouchaud, Marc Potters, et al. Rotational invariant estimator for general noisy matrices. *IEEE Trans. Information Theory*, 62(12):7475–7490, 2016.
- [11] Joël Bun, Jean-Philippe Bouchaud, and Marc Potters. Cleaning large correlation matrices: tools from random matrix theory. *Physics Reports*, 666:1–109, 2017.
- [12] Tony Cai, Jianqing Fan, and Tiefeng Jiang. Distributions of angles in random packing on spheres. *The Journal of Machine Learning Research*, 14(1):1837–1864, 2013.
- [13] Dami Choi, Christopher J Shallue, Zachary Nado, Jaehoon Lee, Chris J Maddison, and George E Dahl. On empirical comparisons of optimizers for deep learning. *arXiv preprint arXiv:1910.05446*, 2019.
- [14] Anna Choromanska, Mikael Henaff, Michael Mathieu, Gérard Ben Arous, and Yann LeCun. The loss surfaces of multilayer networks. In *Artificial Intelligence and Statistics*, pages 192–204, 2015.
- [15] Anna Choromanska, Yann LeCun, and Gérard Ben Arous. Open problem: The landscape of the loss surfaces of multilayer networks. In *Conference on Learning Theory*, pages 1756–1760, 2015.
- [16] Patryk Chrabaszcz, Ilya Loshchilov, and Frank Hutter. A downsampled variant of imagenet as an alternative to the cifar datasets. *arXiv preprint arXiv:1707.08819*, 2017.
- [17] Thomas M Cover and Joy A Thomas. *Elements of information theory*. John Wiley & Sons, 2012.
- [18] Yann N Dauphin, Razvan Pascanu, Caglar Gulcehre, Kyunghyun Cho, Surya Ganguli, and Yoshua Bengio. Identifying and attacking the saddle point problem in high-dimensional non-convex optimization. In *Advances in neural information processing systems*, pages 2933–2941, 2014.

- [19] Adina Roxana Feier. *Methods of proof in random matrix theory*. PhD thesis, Harvard University, 2012.
- [20] Jacob Gardner, Geoff Pleiss, Kilian Q Weinberger, David Bindel, and Andrew G Wilson. Gpytorch: Blackbox matrix-matrix Gaussian process inference with GPU acceleration. In *Advances in Neural Information Processing Systems*, pages 7576–7586, 2018.
- [21] Behrooz Ghorbani, Shankar Krishnan, and Ying Xiao. An investigation into neural net optimization via Hessian eigenvalue density. *arXiv preprint arXiv:1901.10159*, 2019.
- [22] Noah Golmant, Nikita Vemuri, Zhewei Yao, Vladimir Feinberg, Amir Gholami, Kai Rothauge, Michael W Mahoney, and Joseph Gonzalez. On the computational inefficiency of large batch sizes for stochastic gradient descent. *arXiv preprint arXiv:1811.12941*, 2018.
- [23] Gene H Golub and Gérard Meurant. Matrices, moments and quadrature. *Pitman Research Notes in Mathematics Series*, pages 105–105, 1994.
- [24] Gene H Golub and Charles F Van Loan. *Matrix computations*, volume 3. JHU press, 2012.
- [25] Friedrich Götze, A Naumov, and A Tikhomirov. Semicircle law for a class of random matrices with dependent entries. *arXiv preprint arXiv:1211.0389*, 2012.
- [26] Priya Goyal, Piotr Dollár, Ross Girshick, Pieter Noordhuis, Lukasz Wesolowski, Aapo Kyrola, Andrew Tulloch, Yangqing Jia, and Kaiming He. Accurate, large minibatch sgd: Training imagenet in 1 hour. *arXiv preprint arXiv:1706.02677*, 2017.
- [27] Diego Granziol and Stephen Roberts. An information and field theoretic approach to the grand canonical ensemble, 2017.
- [28] Diego Granziol, Xingchen Wan, Timur Garipov, Dmitry Vetrov, and Stephen Roberts. Mlrg deep curvature. *arXiv preprint arXiv:1912.09656*, 2019.
- [29] Guy Gur-Ari, Daniel A Roberts, and Ethan Dyer. Gradient descent happens in a tiny subspace. *arXiv preprint arXiv:1812.04754*, 2018.
- [30] Walid Hachem, Philippe Loubaton, Jamal Najim, and Pascal Vallet. On bilinear forms based on the resolvent of large random matrices. In *Annales de l’IHP Probabilités et statistiques*, volume 49, pages 36–63, 2013.
- [31] Sepp Hochreiter and Jürgen Schmidhuber. Flat minima. *Neural Computation*, 9(1):1–42, 1997.
- [32] Elad Hoffer, Itay Hubara, and Daniel Soudry. Train longer, generalize better: closing the generalization gap in large batch training of neural networks. In *Advances in Neural Information Processing Systems*, pages 1731–1741, 2017.
- [33] Michael F Hutchinson. A stochastic estimator of the trace of the influence matrix for Laplacian smoothing splines. *Communications in Statistics-Simulation and Computation*, 19(2):433–450, 1990.
- [34] Sergey Ioffe and Christian Szegedy. Batch normalization: Accelerating deep network training by reducing internal covariate shift. *arXiv preprint arXiv:1502.03167*, 2015.
- [35] Prateek Jain, Praneeth Netrapalli, Sham M Kakade, Rahul Kidambi, and Aaron Sidford. Parallelizing stochastic gradient descent for least squares regression: mini-batching, averaging, and model misspecification. *The Journal of Machine Learning Research*, 18(1):8258–8299, 2017.
- [36] Stanisław Jastrzębski, Zachary Kenton, Devansh Arpit, Nicolas Ballas, Asja Fischer, Yoshua Bengio, and Amos Storkey. Three factors influencing minima in SGD. *arXiv preprint arXiv:1711.04623*, 2017.
- [37] Stanisław Jastrzębski, Zachary Kenton, Nicolas Ballas, Asja Fischer, Yoshua Bengio, and Amos Storkey. On the relation between the sharpest directions of DNN loss and the SGD step length. 2018.
- [38] Kenji Kawaguchi. Deep learning without poor local minima. In *Advances in neural information processing systems*, pages 586–594, 2016.
- [39] Nitish Shirish Keskar, Dheevatsa Mudigere, Jorge Nocedal, Mikhail Smelyanskiy, and Ping Tak Peter Tang. On large-batch training for deep learning: Generalization gap and sharp minima. *arXiv preprint arXiv:1609.04836*, 2016.
- [40] Diederik P Kingma and Jimmy Ba. Adam: A method for stochastic optimization. *arXiv preprint arXiv:1412.6980*, 2014.

- [41] Alex Krizhevsky. One weird trick for parallelizing convolutional neural networks. *arXiv preprint arXiv:1404.5997*, 2014.
- [42] Hao Li, Zheng Xu, Gavin Taylor, and Tom Goldstein. Visualizing the loss landscape of neural nets. *arXiv preprint arXiv:1712.09913*, 2017.
- [43] Yuanzhi Li, Colin Wei, and Tengyu Ma. Towards explaining the regularization effect of initial large learning rate in training neural networks. In *Advances in Neural Information Processing Systems*, pages 11669–11680, 2019.
- [44] Ilya Loshchilov and Frank Hutter. Decoupled weight decay regularization. *arXiv preprint arXiv:1711.05101*, 2017.
- [45] David JC MacKay. *Information theory, inference and learning algorithms*. Cambridge university press, 2003.
- [46] James Martens. Deep learning via Hessian-free optimization. In *ICML*, volume 27, pages 735–742, 2010.
- [47] James Martens. New insights and perspectives on the natural gradient method. *arXiv preprint arXiv:1412.1193*, 2014.
- [48] James Martens. *Second-order optimization for neural networks*. PhD thesis, University of Toronto, 2016. URL http://www.cs.toronto.edu/~jmartens/docs/thesis_phd_martens.pdf.
- [49] James Martens and Roger Grosse. Optimizing neural networks with Kronecker-factored approximate curvature. In *International conference on machine learning*, pages 2408–2417, 2015.
- [50] James Martens and Ilya Sutskever. Training deep and recurrent networks with Hessian-free optimization. In *Neural networks: Tricks of the trade*, pages 479–535. Springer, 2012.
- [51] Gérard Meurant and Zdeněk Strakoš. The Lanczos and conjugate gradient algorithms in finite precision arithmetic. *Acta Numerica*, 15:471–542, 2006.
- [52] Yurii Nesterov. *Introductory lectures on convex optimization: A basic course*, volume 87. Springer Science & Business Media, 2013.
- [53] Sean O’Rourke et al. A note on the marchenko-pastur law for a class of random matrices with dependent entries. *Electronic Communications in Probability*, 17, 2012.
- [54] Vardan Papyan. The full spectrum of deep net Hessians at scale: Dynamics with sample size. *arXiv preprint arXiv:1811.07062*, 2018.
- [55] Razvan Pascanu and Yoshua Bengio. Revisiting natural gradient for deep networks. *arXiv preprint arXiv:1301.3584*, 2013.
- [56] Adam Paszke, Sam Gross, Soumith Chintala, Gregory Chanan, Edward Yang, Zachary DeVito, Zeming Lin, Alban Desmaison, Luca Antiga, and Adam Lerer. Automatic differentiation in Pytorch. 2017.
- [57] Barak A Pearlmutter. Fast exact multiplication by the Hessian. *Neural computation*, 6(1): 147–160, 1994.
- [58] Jeffrey Pennington and Yasaman Bahri. Geometry of neural network loss surfaces via random matrix theory. In *Proceedings of the 34th International Conference on Machine Learning-Volume 70*, pages 2798–2806. JMLR. org, 2017.
- [59] Jeffrey Pennington and Pratik Worah. The spectrum of the fisher information matrix of a single-hidden-layer neural network. In *Advances in Neural Information Processing Systems*, pages 5410–5419, 2018.
- [60] Farbod Roosta-Khorasani and Uri Ascher. Improved bounds on sample size for implicit matrix trace estimators. *Foundations of Computational Mathematics*, 15(5):1187–1212, 2015.
- [61] Farbod Roosta-Khorasani and Michael W Mahoney. Sub-sampled newton methods ii: Local convergence rates. *arXiv preprint arXiv:1601.04738*, 2016.
- [62] Levent Sagun, Léon Bottou, and Yann LeCun. Eigenvalues of the Hessian in deep learning: Singularity and beyond. *arXiv preprint arXiv:1611.07476*, 2016.
- [63] Levent Sagun, Utku Evci, V Ugur Guney, Yann Dauphin, and Leon Bottou. Empirical analysis of the Hessian of over-parametrized neural networks. *arXiv preprint arXiv:1706.04454*, 2017.

- [64] Christopher J Shallue, Jaehoon Lee, Joseph Antognini, Jascha Sohl-Dickstein, Roy Frostig, and George E Dahl. Measuring the effects of data parallelism on neural network training. *arXiv preprint arXiv:1811.03600*, 2018.
- [65] Karen Simonyan and Andrew Zisserman. Very deep convolutional networks for large-scale image recognition. *arXiv preprint arXiv:1409.1556*, 2014.
- [66] Charles Stein. A bound for the error in the normal approximation to the distribution of a sum of dependent random variables. In *Proceedings of the Sixth Berkeley Symposium on Mathematical Statistics and Probability, Volume 2: Probability Theory*, pages 583–602, Berkeley, Calif., 1972. University of California Press.
- [67] Cecilia Summers and Michael J Dinneen. Four things everyone should know to improve batch normalization. *arXiv preprint arXiv:1906.03548*, 2019.
- [68] Terence Tao. *Topics in random matrix theory*, volume 132. American Mathematical Soc., 2012.
- [69] Oriol Vinyals and Daniel Povey. Krylov subspace descent for deep learning. In *Artificial Intelligence and Statistics*, pages 1261–1268, 2012.
- [70] Hermann Weyl. Das asymptotische verteilungsgesetz der eigenwerte linearer partieller differentialgleichungen (mit einer anwendung auf die theorie der hohlraumstrahlung). *Mathematische Annalen*, 71(4):441–479, Dec 1912. ISSN 1432-1807.
- [71] Lei Wu, Zhanxing Zhu, et al. Towards understanding generalization of deep learning: Perspective of loss landscapes. *arXiv preprint arXiv:1706.10239*, 2017.
- [72] Sergey Zagoruyko and Nikos Komodakis. Wide residual networks. *arXiv preprint arXiv:1605.07146*, 2016.
- [73] Guodong Zhang, Lala Li, Zachary Nado, James Martens, Sushant Sachdeva, George Dahl, Chris Shallue, and Roger B Grosse. Which algorithmic choices matter at which batch sizes? insights from a noisy quadratic model. In *Advances in Neural Information Processing Systems*, pages 8194–8205, 2019.

A Proof of Main Result

A full proof of Theorem 2, which rests heavily on disparate yet known results in the literature [25, 3, 11], once introducing all the relevant transforms and nomenclature to the non expert reader, would in addition to extensively duplication prior work span many dozens of pages. We hence adopt an alternative proof strategy. Instead, to make the proof understandable and relateable to a machine learning audience, for which this work is intended, we introduce a minimum amount of necessary random matrix theory background. We then prove Theorem 2, but under the stronger assumptions that the elements of the noise matrix are i.i.d Gaussian (the Gaussian Orthogonal Ensemble). To understand why this makes sense, we consider the key ingredients of the proof

- The noise matrix converges to the semi-circle law;
- the spectral perturbation low rank empirical Hessian by the noise matrix can be computed analytically using perturbation theory;
- By Lemma 2, the scaling relationships which characterise the extent of the noise perturbation as a function of batch size can be analysed.

Hence the only difference between the simplified proof and Theorem 2, is that we have more general conditions for the convergence semi circle law, which are detailed extensively in in Götze et al. [25]. The other two key components proceed in an identical fashion.

A.1 Background

Following the notation of [11] the resolvent of a matrix H is defined as

$$G_H(z) = (zI_N - H)^{-1} \quad (18)$$

with $z = x + i\eta \in \mathbb{C}$. The normalised trace operator of the resolvent, in the $N \rightarrow \infty$ limit

$$\mathcal{S}_N(z) = \frac{1}{N} \text{Tr}[G_H(z)] \xrightarrow{N \rightarrow \infty} \mathcal{S}(z) = \int \frac{\rho(u)}{z - u} du \quad (19)$$

is known as the Stieltjes transform of ρ . The functional inverse of the Stieltjes transform, is denoted the blue function $\mathcal{B}(\mathcal{S}(z)) = z$. The \mathcal{R} transform is defined as

$$\mathcal{R}(w) = \mathcal{B}(w) - \frac{1}{w} \quad (20)$$

crucially for our calculations, it is known that the \mathcal{R} transform of the Wigner ensemble is

$$\mathcal{R}_W(z) = \sigma^2 z \quad (21)$$

Definition A.1. Let $\{Y_i\}$ and $\{Z_{ij}\}_{1 \leq i \leq j}$ be two real-valued families of zero mean, i.i.d random variables, Furthermore suppose that $\mathbb{E}Z_{12}^2 = 1$ and for each $k \in \mathbb{N}$

$$\max(E|Z_{12}^k|, E|Y_1|^k) < \infty \quad (22)$$

Consider an $n \times n$ symmetric matrix M_n , whose entries are given by

$$\begin{cases} M_n(i, i) = Y_i \\ M_n(i, j) = Z_{ij} = M_n(j, i), \quad \text{if } i > j \end{cases} \quad (23)$$

The Matrix M_n is known as a real symmetric Wigner matrix.

Theorem 4. Let $\{M_n\}_{n=1}^\infty$ be a sequence of Wigner matrices, and for each n denote $X_n = M_n/\sqrt{n}$. Then μ_{X_n} , converges weakly, almost surely to the semi circle distribution,

$$\sigma(x)dx = \frac{1}{2\pi} \sqrt{4 - x^2} \mathbf{1}_{|x| \leq 2} \quad (24)$$

the property of freeness for non commutative random matrices can be considered analogously to the moment factorisation property of independent random variables. The normalized trace operator, which is equal to the first moment of the spectral density

$$\psi(H) = \frac{1}{N} \text{Tr}H = \frac{1}{N} \sum_{i=1}^N \lambda_i = \int_{\lambda \in \mathcal{D}} d\mu(\lambda) \lambda \quad (25)$$

We say matrices A & B for which $\psi(A) = \psi(B) = 0^8$ are free if they satisfy for any integers $n_1 \dots n_k$ with $k \in \mathbb{N}^+$

$$\psi(A^{n_1} B^{n_2} A^{n_3} B^{n_4}) = \psi(A^{n_1}) \psi(B^{n_2}) \psi(A^{n_3}) \psi(B^{n_4}) \quad (26)$$

A.2 Derivation of main result

Theorem 5. The extremal eigenvalues $[\lambda'_1, \lambda'_P]$ of the matrix sum $\mathbf{A} + \mathbf{B}/\sqrt{P}$, where $\mathbf{A} \in \mathbb{R}^{P \times P}$ is a matrix of finite rank r with extremal eigenvalues $[\lambda_1, \lambda_P]$ and $\mathbf{B} \in \mathbb{R}^{P \times P}$ is a GOE matrix with element variance σ_ϵ^2 are given by

$$\lambda'_1 = \begin{cases} \lambda_1 + \frac{\sigma_\epsilon^2}{\lambda_1}, & \text{if } \lambda_1 > \sigma_\epsilon \\ 2\sigma_\epsilon, & \text{otherwise} \end{cases}, \quad \lambda'_P = \begin{cases} \lambda_P + \frac{\sigma_\epsilon^2}{\lambda_P}, & \text{if } \lambda_P < -\sigma_\epsilon \\ -2\sigma_\epsilon, & \text{otherwise} \end{cases} \quad (27)$$

The Stieltjes transform of Wigners semi circle law, can be written as [68]

$$\mathcal{S}_W(z) = \frac{z \pm \sqrt{z^2 - 4\sigma^2}}{2\sigma^2} \quad (28)$$

from the definition of the Blue transform, we hence have

$$\begin{aligned} z &= \frac{\mathcal{B}_W(z) \pm \sqrt{\mathcal{B}_W^2(z) - 4\sigma^2}}{2\sigma^2} \\ (2\sigma^2 z - \mathcal{B}_W(z))^2 &= \mathcal{B}_W^2(z) - 4\sigma^2 \\ \therefore \mathcal{B}_W(z) &= \frac{1}{z} + \sigma^2 z \\ \therefore \mathcal{R}_W(z) &= \sigma^2 z \end{aligned} \quad (29)$$

⁸We can always consider the transform $A - \psi(A)I$

Computing the \mathcal{R} transform of the rank 1 matrix H_{true} , with largest non-trivial eigenvalue β , on the effect of the spectrum of a matrix A , using the Stieltjes transform we easily find following [11] that

$$\mathcal{S}_{H_{true}}(u) = \frac{1}{N} \frac{1}{u - \beta} + \left(1 - \frac{1}{N}\right) \frac{1}{u} = \frac{1}{u} \left[1 + \frac{1}{N} \frac{\beta}{1 - u^{-1}\beta}\right] \quad (30)$$

We can use perturbation theory similar to in equation 29 to find the blue transform which to leading order gives

$$\begin{aligned} \mathcal{B}_{H_{true}}(\omega) &= \frac{1}{\omega} + \frac{\beta}{N(1 - \omega\beta)} + \mathcal{O}(N^{-2}) \\ \mathcal{R}_{H_{true}}(\omega) &= \frac{\beta}{N(1 - \omega\beta)} + \mathcal{O}(N^{-2}) \end{aligned} \quad (31)$$

setting $\omega = \mathcal{S}_M(z)$

$$z = \mathcal{B}_{H_{true}}(\mathcal{S}_M(z)) + \frac{\beta}{N(1 - \beta\mathcal{S}_M(z))} + \mathcal{O}(N^{-2}) \quad (32)$$

using the ansatz of $\mathcal{S}_M(z) = \mathcal{S}_0(z) + \frac{\mathcal{S}_1(z)}{N} + \mathcal{O}(N^{-2})$ we find that $\mathcal{S}_0(z) = \mathcal{S}_{\epsilon(w)}(z)$ and using that $\mathcal{B}'_M(z) = 1/g'(z)$, we conclude that

$$\mathcal{S}_1(z) = -\frac{\beta \mathcal{S}'_{\epsilon(w)}(z)}{1 - \mathcal{S}_{\epsilon(w)}(z)\beta} \quad (33)$$

and hence

$$\mathcal{S}_M(z) \approx \mathcal{S}_{\epsilon(w)}(z) - \frac{1}{N} \frac{\beta \mathcal{S}'_{\epsilon(w)}(z)}{1 - \mathcal{S}_{\epsilon(w)}(z)\beta} \quad (34)$$

and hence in the large N limit the correction only survives if $\mathcal{S}_{\epsilon(w)}(z) = 1/\beta$

$$\begin{aligned} \mathcal{S}_{\epsilon(w)}(z) &= \frac{1}{\beta} \\ \frac{2\sigma^2}{\beta} &= z \pm \sqrt{z^2 - 4\sigma^2} \\ \therefore z &= \beta + \frac{\sigma^2}{\beta} \end{aligned} \quad (35)$$

clearly for $\beta \rightarrow -\beta$ we have

$$z = -\beta - \frac{\sigma^2}{\beta} \quad (36)$$

The variance per element is a function of the batch size B and the size of the empirical dataset N , as given by Lemma 2 Furthermore, unravelling the dependence in P due to the definition of the Wigner matrix in Section A leads to Theorem 2.

B Low Rank Approximation

One of the key ingredients to proving 2, as shown in 2 is the use of perturbation theory. This requires either the noise matrix or the full empirical Hessian to be low rank. In our work, we consider the empirical Hessian to be low rank. The rank degeneracy of small neural networks has already been discovered and discussed in Sagun et al. [63] and reported for larger networks using spectral approximations in Ghorbani et al. [21], Pappayan [54]. We provide extensive experimental validation for both the VGG-16 and PreResNet-110 on the CIFAR-100 datasets in Sections B.1 and B.2, along with a theoretical argument and rank bound for feed forward neural networks with cross entropy loss in Section B.3.

Experimental Setup: Given that Hessians have P^2 elements with a full inversion cost of $\mathcal{O}(P^3)$ which is infeasible for large neural networks. Counting the number of 0 eigenvalues (which sets the degeneracy) is not feasible in this manner. Furthermore, there would still be issues with numerical precision, so a threshold would be needed for accurate counting. Hence, based on our understanding of the Lanczos algorithm, discussed in section D, we propose an alternative method. We know that m steps of the Lanczos method, gives us an m -moment matched spectral approximation of the moments of $v^T H v$, where in expectation over the set of zero mean unit variance random vectors this is equal to the spectral density of H . Each eigenvalue, eigenvector pair estimated by the Lanczos algorithm is called a Ritz-value/Ritz-vector. We hence take $m \gg 1$, where typically and for consistency we take $m = 100$ in our experiments. We then take the Ritz value closest to the origin and take that as a proxy for the 0 eigenvalue and report its weight. One weakness of this method is that for a large value of m , since the Lanczos algorithm finds a discrete moment matched spectral algorithm, is that the spectral mass near the origin, may split into multiple components and counting the largest thereof or closest to the origin may not be sufficient. We note this problem both for the PreResNet-110 and VGG-16 on the CIFAR-100 dataset shown in Figure 9. Significant drops in degeneracy occur at various points in training and occur in tandem with significant changes in the absolute value of the Ritz value of minimal magnitude. This suggests the aforementioned splitting phenomenon is occurring. This issue is not present in the calculation of the generalised Gauss Newton, as the spectrum is constrained to be positive definite, so there is a limit to the extent of splitting that may occur. In order to remedy this problem, for the Hessian we calculate the combination of the two closest Ritz values around the centre and combine their mass. We consider this mass and the weighted average of their values as the degenerate mass. An alternative approach could be to kernel smooth the Ritz weights at their values, but this would involve another arbitrary hyper-parameter σ .

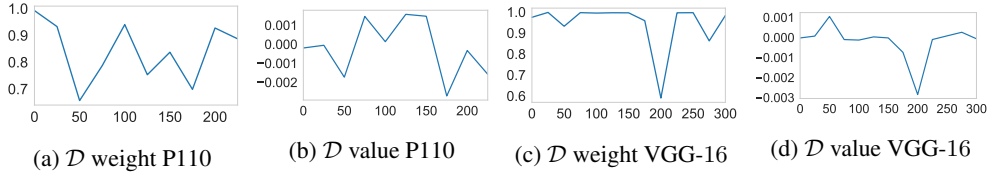


Figure 9: Rank degeneracy \mathcal{D} evolution throughout training using the VGG-16 and PreResNet-110 on the CIFAR-100 dataset, the weight corresponds to the spectral mass of the Ritz value \mathcal{D}

B.1 VGG16

For the VGG-16, which forms the reference model for this paper, we see that for both the generalised Gauss-Newton (shown in Figure 10a) and the Hessian (shown in Figure 10c) that the rank degeneracy is extremely high. For the GGN, the magnitude of the Ritz value which we take to be the origin, is extremely close to the threshold for GPU precision, as shown in Figure 10b. For the Hessian, for which we combine the two smallest absolute value Ritz values, we have as expected an even larger spectral degeneracy. The weighted average, also gives a value very close to 0, as shown in Figure 10d. Although the combined weighted average is much closer to the origin, than that of the lone spectral peak, shown in Figure 9, which indicates splitting, we do not get as close to the GPU precision threshold.

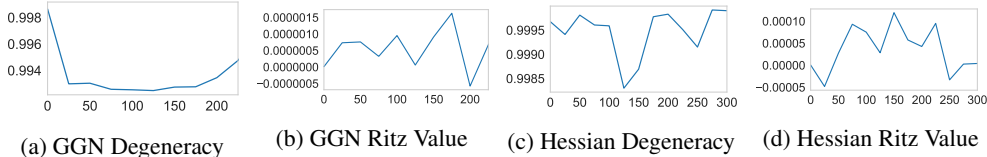


Figure 10: Rank degeneracy evolution throughout training using the VGG-16 on the CIFAR-100 dataset, total training 225 epochs, the Ritz value corresponds to the value of the node which we assign to 0

B.2 PreResNet110

We repeat the same experiments in section B.1 for the preactivate residual network with 110 layers, on the same dataset. The slight subtlety is that as explained in Section H, we can calculate the spectra in both batch normalisation and evaluation mode. Hence we report results for both, with the main finding, that the empirical Hessian spectra are consistent with large rank degeneracy.

B.2.1 Generalised Gauss Newton

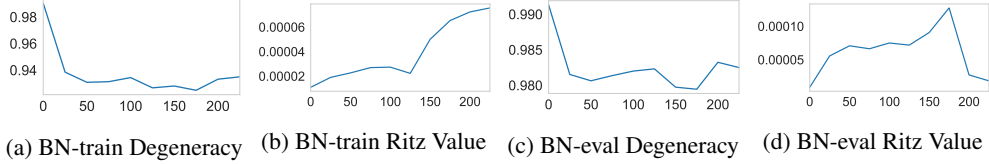


Figure 11: Generalised Gauss Newton rank degeneracy evolution throughout training using the PreResNet-110 on the CIFAR-100 dataset, total training 225 epochs, the Ritz value corresponds to the value of the node which we assign to 0

B.2.2 Hessian

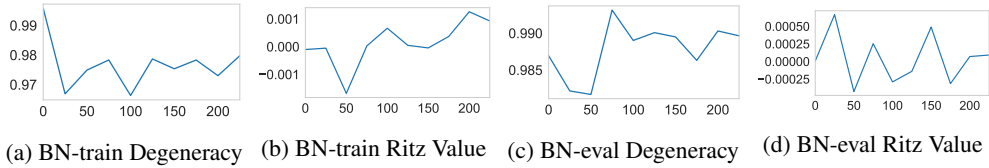


Figure 12: Hessian rank degeneracy evolution throughout training using the PreResNet-110 on the CIFAR-100 dataset, total training 225 epochs, the Ritz value corresponds to the value of the node which we assign to 0

B.3 Theoretical argument for Feed Forward Networks

For a feed forward neural network, by considering the paths in the network, the input to neuron m_k for a given data point \mathbf{x} is given by $\sum_{n_j}^{N_1} \sum_i^{d_x} x_i \mathbf{w}_{x_i, n_j} \mathbf{w}_{n_j, m_k}$, where N_1 is the number of neurons in layer 1. For a neural network $d - 1$ hidden layers

$$h_m = \prod_{l=1}^{d-1} \sum_{n_{i,l}=1}^{N_{i,l}} \sum_i^{d_x} \mathbf{x}_i \mathbf{w}_{n_{i,l}, n_{i,l+1}} \delta(n_{i,d} = m) \quad (37)$$

where $n_{i,l_1} = x_i$ and we fix to the desired output class, through the delta function. The Hessian of the loss in the small loss limit tends to

$$\frac{\partial^2 \ell(h(\mathbf{x}_i; \mathbf{w}), \mathbf{y}_i)}{\partial w_{\phi, \kappa} \partial w_{\theta, \nu}} \rightarrow - \sum_{m \neq c} \exp(h_m) \left[\frac{\partial^2 h_m}{\partial w_{\phi, \kappa} \partial w_{\theta, \nu}} + \frac{\partial h_m}{\partial w_{\phi, \kappa}} \frac{\partial h_m}{\partial w_{\theta, \nu}} \right] \quad (38)$$

$$\begin{aligned} \left[\frac{\partial^2 h_m}{\partial w_{\phi, \kappa} \partial w_{\theta, \nu}} + \frac{\partial h_m}{\partial w_{\phi, \kappa}} \frac{\partial h_m}{\partial w_{\theta, \nu}} \right] &= \prod_{l=1}^{d-1} \sum_{n_{i,l} \neq [(\phi, \kappa), (\theta, \nu)]}^{N_{i,l}} \sum_i^{d_x} \mathbf{x}_i \mathbf{w}_{n_{i,l}, n_{i,l+1}} \delta(n_{i,d} = m) \\ &+ \left(\prod_{l=1}^{d-1} \sum_{n_{i,l} \neq (\theta, \nu)}^{N_{i,l}} \sum_i^{d_x} \mathbf{x}_i \mathbf{w}_{n_{i,l}, n_{i,l+1}} \delta(n_{i,d} = m) \right) \left(\prod_{l=1}^{d-1} \sum_{n_{j,l} \neq (\phi, \kappa)}^{N_{j,l}} \sum_i^{d_x} \mathbf{x}_i \mathbf{w}_{n_{j,l}, n_{j,l+1}} \delta(n_{j,d} = m) \right) \end{aligned} \quad (39)$$

Each product of weights contributes an object of rank-1 (as shown in section ??). Furthermore, the rank of a product is the minimum of the constituent ranks, i.e $\text{rank}(AB) = \min \text{rank}(A, B)$. Hence equation 39 is rank bounded by a $2(\sum_l N_l + d_x)$, where N_l is the total numbers of neurons in the network. By rewriting the loss per-sample and repeating the same arguments and including the class factor

$$\frac{\partial^2 \ell}{\partial w_k \partial w_l} = -\frac{\partial^2 h_{q(i)}}{\partial w_k \partial w_l} + \frac{\sum_j \exp(h_j) \sum_i \exp(h_i) (\frac{\partial^2 h_i}{\partial w_k \partial w_l} + \frac{\partial h_i}{\partial w_k} \frac{\partial h_i}{\partial w_l}) - \sum_i \exp(h_i) \frac{\partial h_i}{\partial w_k} \sum_j \frac{\partial h_j}{\partial w_l} \exp(h_j)}{[\sum_j \exp(h_j)]^2} \quad (40)$$

We obtain a rank bound of $4d_y(\sum_l N_l + d_x)$. To give some context, along with a practical application of a real network and dataset, for the CIFAR-10 dataset, the VGG-16 [65] contains 1.6×10^7 parameters, the number of classes is 10 and the total number of neurons is 13, 416 and hence the bound gives us a spectral peak at the origin of at least $1 - \frac{577.600}{1.6 \times 10^7} = 0.9639$. We give extensive experimental validation for the low rank nature of the empirical Hessian in Section B.

C Alternative learning rate schedules and initialisation distance importance

One implicit assumption in Section 5 is that the largest learning rate which trains stably gives the best result. This informs our work as to how we should scale this rate as the batch size is increased. However it makes sense to consider how alternative more conservative scaling rules might fare and whether they impact performance. In this section we also consider whether increased distance from Initialisation, as posited in [32] is relevant for generalisation.

We do this for the VGG-16 on the CIFAR-100 dataset. Against a baseline validation accuracy of 65.82% for $B = 128$. For the $B = 1024$ case, our theoretically justified linearly increased learning rate of 0.08 gives an accuracy of 64.35%, whereas using the square root rule [32] suggestion of 0.028 only gives 61.08%, we note from Figure 2 that there are many well separated outliers. On the held out test set, the linear scaling solution has an error of 34.64% and a distance of 145.76 in L_2 norm from the initialisation, whereas the square root scaled solution has an error of 37.55% and a distance of 67.44 from initialization. This indicates that as argued in Hoffer et al. [32] that distance from initialization seems to play an important role for generalisation.

We test this further by looking at the initialisation distance across the set of similar test performing solutions for a constant learning rate to batch size ratio. Interestingly for the VGG-16 without batch normalisation as shown in Figure 3a there is a strong link between initialisation distance in L_2 norm and the test error. This relationship is much weaker and much smaller in magnitude when batch normalisation is utilised, as shown in Figure 3b. We even see the initialisation distance increasing as test error also increases.

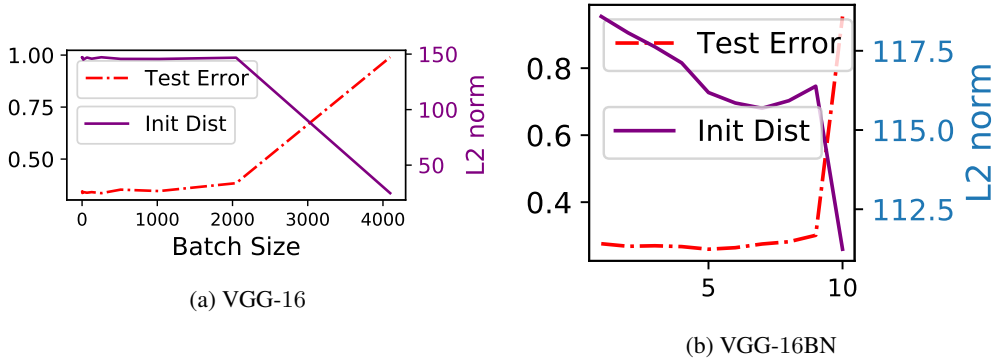


Figure 13: Test error as a function of initialisation distance for both the VGG-16 and VGG-16BN, for the CIFAR-100 dataset. Learning rate is scaled linearly with batch size.

D Lanczos algorithm

In order to empirically analyse properties of modern neural network spectra with tens of millions of parameters $N = \mathcal{O}(10^7)$, we use the Lanczos algorithm [51], provided for deep learning by Granziol et al. [28]. It requires Hessian vector products, for which we use the Pearlmutter trick [57] with computational cost $\mathcal{O}(NP)$, where N is the dataset size and P is the number of parameters. Hence for m steps the total computational complexity including re-orthogonalisation is $\mathcal{O}(NPM)$ and memory cost of $\mathcal{O}(Pm)$. In order to obtain accurate spectral density estimates we re-orthogonalise at every step [51]. We exploit the relationship between the Lanczos method and Gaussian quadrature, using random vectors to allow us to learn a discrete approximation of the spectral density. A quadrature rule is a relation of the form,

$$\int_a^b f(\lambda)d\mu(\lambda) = \sum_{j=1}^M \rho_j f(t_j) + R[f] \quad (41)$$

for a function f , such that its Riemann-Stieltjes integral and all the moments exist on the measure $d\mu(\lambda)$, on the interval $[a, b]$ and where $R[f]$ denotes the unknown remainder. The nodes t_j of the Gauss quadrature rule are given by the Ritz values and the weights (or mass) ρ_j by the squares of the first elements of the normalized eigenvectors of the Lanczos tri-diagonal matrix [23]. The main properties of the Lanczos algorithm are summarized in the theorems 6,7

Theorem 6. *Let $H^{N \times N}$ be a symmetric matrix with eigenvalues $\lambda_1 \geq \dots \geq \lambda_n$ and corresponding orthonormal eigenvectors z_1, \dots, z_n . If $\theta_1 \geq \dots \geq \theta_m$ are the eigenvalues of the matrix T_m obtained after m Lanczos steps and q_1, \dots, q_k the corresponding Ritz eigenvectors then*

$$\begin{aligned} \lambda_1 &\geq \theta_1 \geq \lambda_1 - \frac{(\lambda_1 - \lambda_n) \tan^2(\theta_1)}{(c_{k-1}(1 + 2\rho_1))^2} \\ \lambda_n &\leq \theta_k \leq \lambda_m + \frac{(\lambda_1 - \lambda_n) \tan^2(\theta_1)}{(c_{k-1}(1 + 2\rho_1))^2} \end{aligned} \quad (42)$$

where c_k is the chebyshev polyomial of order k

Proof: see [24].

Theorem 7. *The eigenvalues of T_k are the nodes t_j of the Gauss quadrature rule, the weights w_j are the squares of the first elements of the normalized eigenvectors of T_k*

Proof: See [23]. The first term on the RHS of equation 41 using Theorem 7 can be seen as a discrete approximation to the spectral density matching the first m moments $v^T H^m v$ [23, 24], where v is the initial seed vector. Using the expectation of quadratic forms, for zero mean, unit variance random vectors, using the linearity of trace and expectation

$$\mathbb{E}_v \text{Tr}(v^T H^m v) = \text{Tr} \mathbb{E}_v(v v^T H^m) = \text{Tr}(H^m) = \sum_{i=1}^N \lambda_i = N \int_{\lambda \in \mathcal{D}} \lambda d\mu(\lambda) \quad (43)$$

The error between the expectation over the set of all zero mean, unit variance vectors v and the monte carlo sum used in practice can be bounded [33, 60]. However in the high dimensional regime $N \rightarrow \infty$, we expect the squared overlap of each random vector with an eigenvector of H , $|v^T \phi_i|^2 \approx \frac{1}{N} \forall i$, with high probability. This result can be seen by computing the moments of the overlap between Rademacher vectors, containing elements $P(v_j = \pm 1) = 0.5$. Further analytical results for Gaussian vectors have been obtained [12].

E True Loss Surface

As a small aside, in our work we consider the empirical Hessian and the batch Hessian. Another natural object which emerges from our analysis, is the Hessian under the data generating distribution. For P finite and $N \rightarrow \infty$, i.e. $q = P/N \rightarrow 0$, $|\epsilon(\mathbf{w})| \rightarrow 0$ the empirical Hessian would become the true Hessian. However, in deep learning typically the network size eclipses the dataset size by orders of magnitude.⁹ This is similar to considering the perturbations between the true covariance matrix and the noisy sample covariance matrix, extensively studied in mathematics and physics [2, 7, 6].

⁹CIFAR datasets, which have 50,000 examples, are routinely used to train networks with about 50 million parameters.

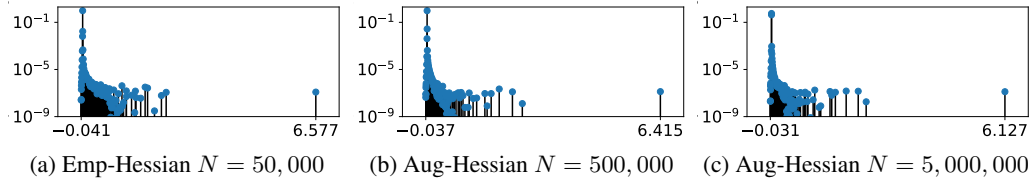


Figure 14: Hessian Spectral Density at epoch 300 , on a VGG-16 on the CIFAR-100 dataset, for different amounts of data-augmentation

As the true Hessian and true risk are un-observable, we consider whether the empirical Hessian provides a valid approximation to the true Hessian, by evaluating the Hessian by artificially increasing the number of samples through the use of data-augmentation, explained in section 3. As shown in Figure 14, the extremal eigenvalues are reduced in size as the sample number is increased, in accordance with Theorem 2.

In order to simulate the effect of increasing the data-set size, we use data augmentation to artificially increase the dataset size, specifically random horizontal flips, 4×4 zero padding and random 32×32 crops and then we use the Pearlmutter trick [57] on the augmented dataset combined with the Lanczos algorithm to estimate the spectral density. While there is clear dependence between the augmented samples and original samples, intuitively we can consider the augmented dataset to be equivalent to an independent set of larger size than the original dataset. This intuition is grounded as training without augmentation leads to significant performance decreases similar to reducing the dataset size. Specifically for the VGG-16 without augmentation we achieve a testing accuracy of 48.8% compared to 72.1% on the CIFAR-100 dataset running the same schedule. We note from Figure 14, that despite a factor of 100 in augmentation, the differences between the most augmented and empirical Hessian are slight. There is a slight reduction in the extremal eigenvalues, but otherwise the general shape remains unaffected. This gives evidence that the true Hessian may be similar to the empirical Hessian.

F Experimental Details

We use the GPU powered Lanczos quadrature algorithm [20, 51], with the Pearlmutter trick [57] for Hessian and GGN vector products, using the PyTorch [56] implementation of both Stochastic Lanczos Quadrature and the Pearlmutter. We then train a 16 Layer VGG CNN [65] with $P = 15291300$ parameters on the CIFAR-100 dataset (45,000 training samples and 5,000 validation samples) using SGD and K-FAC optimisers. For both SGD and K-FAC, we use the following learning rate schedule:

$$\alpha_t = \begin{cases} \alpha_0, & \text{if } \frac{t}{T} \leq 0.5 \\ \alpha_0 \left[1 - \frac{(1-r)(\frac{t}{T} - 0.5)}{0.4} \right], & \text{if } 0.5 < \frac{t}{T} \leq 0.9 \\ \alpha_0 r, & \text{otherwise} \end{cases} \quad (44)$$

We use learning rate ratio $r = 0.01$ and total number of epochs budgeted $T = 300$. We further use momentum $\rho = 0.9$, a weight decay coefficient of 0.0005 and data-augmentation on PyTorch [56]. We further set the inversion frequency to be once per 100 iterations for K-FAC.

G Tiny Batch Sizes

In this section we simply present extended results from section 5, where we include training curves for smaller batch sizes still. The relevant implications are simply that without batch-normalisation, the scaling rules hold until $B = 1$ and with batch-normalisation, potentially due to the need to estimate variances accurately within layers, we typically start to see a degradation of model quality below $B = 8$.

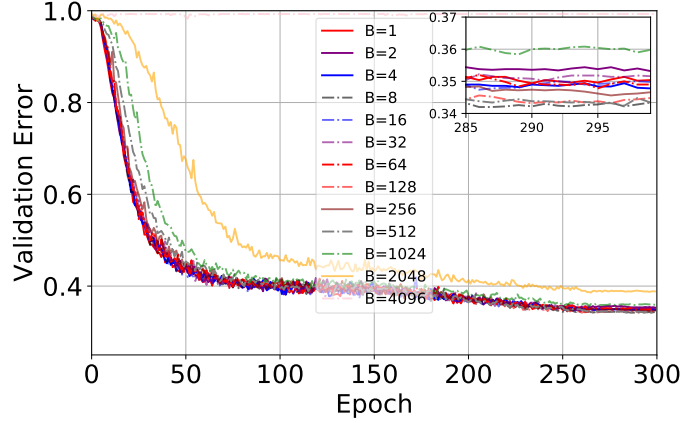


Figure 15: VGG-16 CIFAR-100, No-BN $\alpha_0 = \frac{0.05B}{128}, \gamma = 0$

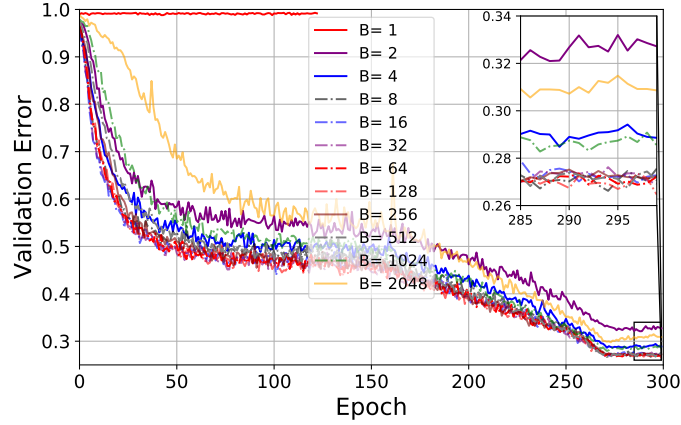


Figure 16: VGG-16BN CIFAR-100, $\alpha_0 = \frac{0.1B}{128}, \gamma = 0.0005$

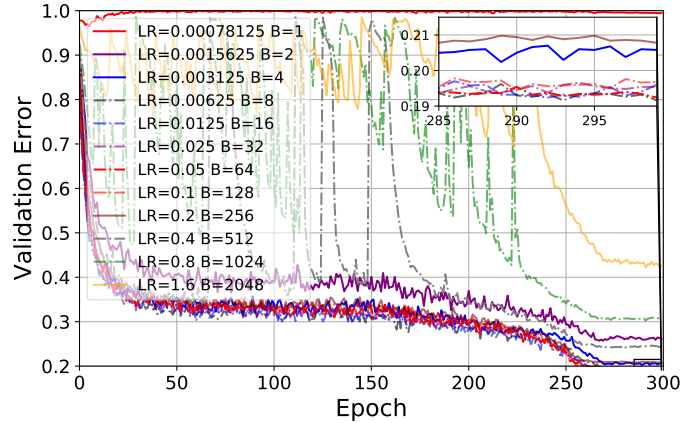


Figure 17: WideResNet- 28×10 CIFAR-100, $\alpha_0 = \frac{0.1B}{128}, \gamma = 0.0005$

H Batch Normalisation Results

Given that the vast majority of image classification are run in conjunction with normalisation methods such as batch normalisation [34] and previous literature observing that batch normalisation suppresses outliers [21] it is important to investigate whether the observations in terms of spectral structure and

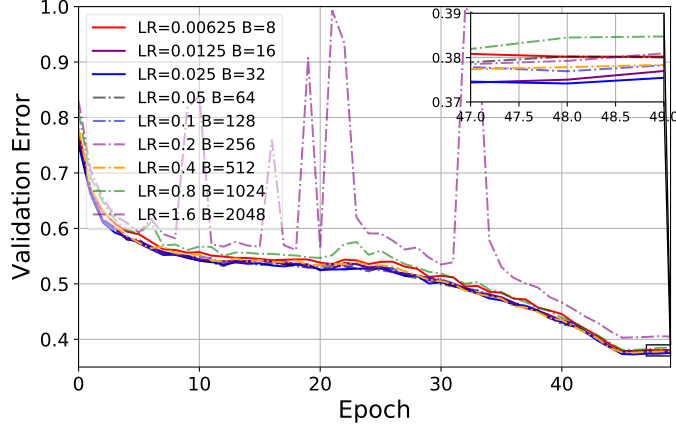


Figure 18: WideResNet-28 \times 10 ImageNet-32, $\alpha_0 = \frac{0.1B}{128}$, $\gamma = 0.0005$

mini-batching effect are in any way invalidated with batch-normalisation. We hence present results on a variety of pre-activated residual networks. We show that the typical spectral density plots in the main text with well separated outliers, a large rank degeneracy and large increase in spectral width with mini-batching are visible also in batch normalised resnets more commonly used in deep learning for both types of batch normalisation mode (explained in the next paragraph).

Technical point on batch norm: Batch-normalisation, as alluded to in the main text function differently during training and during evaluation. When evaluating curvature, we thus have the option of choosing the setting of this functionality. We denote the same properties as during training as batch norm train mode and those during evaluation as batch norm evaluation mode.

H.1 PreResNet110

We look at the generalised Gauss Newton and Hessian of the PreResNet-110 in batch norm evaluation and training mode.

H.1.1 Generalised Gauss Newton - batch normalisation train mode

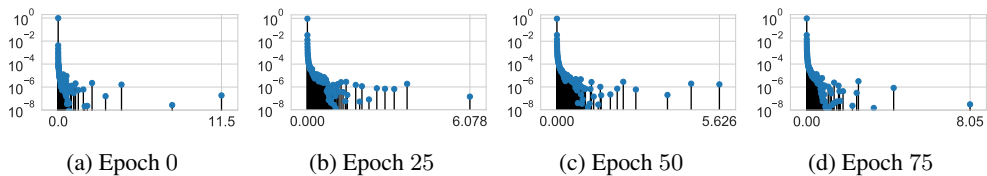


Figure 19: Generalised Gauss Newton full empirical spectrum for the PreResNet-110 on the CIFAR-100 dataset, total training 225 epochs, batch norm train mode

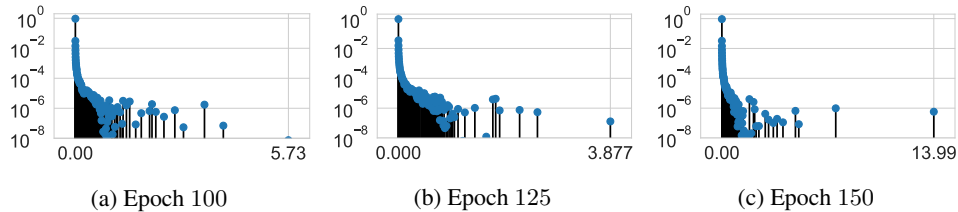


Figure 20: Generalised Gauss Newton full empirical spectrum for the PreResNet-110 on the CIFAR-100 dataset, total training 225 epochs, batch norm train mode

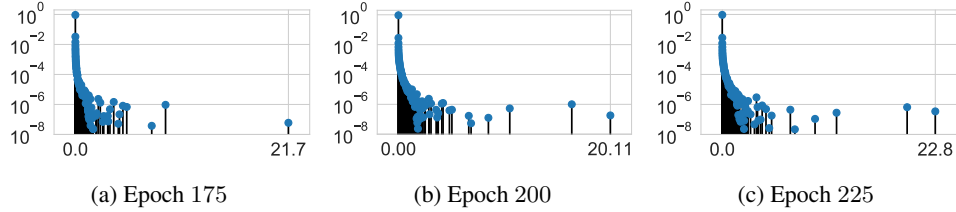


Figure 21: Generalised Gauss Newton full empirical spectrum for the PreResNet-110 on the CIFAR-100 dataset, total training 225 epochs, batch norm train mode

To show similarly that the Generalised Gauss Newton experiences severe spectral broadening when mini-batching, we take the same points in weight space as in Figure 39 but instead take stochastic samples of size $B = 128$, although the results are stochastic, they are stochastic around a significantly broadened spectrum, with some samples shown in Figure 22, for comparison. Where we see significant broadening.

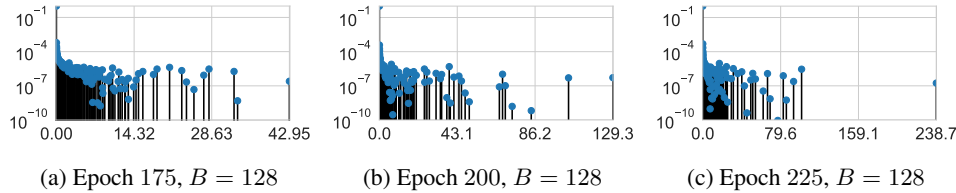


Figure 22: Generalised Gauss Newton full empirical spectrum for the PreResNet-110 on the CIFAR-100 dataset, total training 225 epochs, batch norm train mode, samples taken with a batch of $B = 128$

H.2 Generalised Gauss Newton - Eval

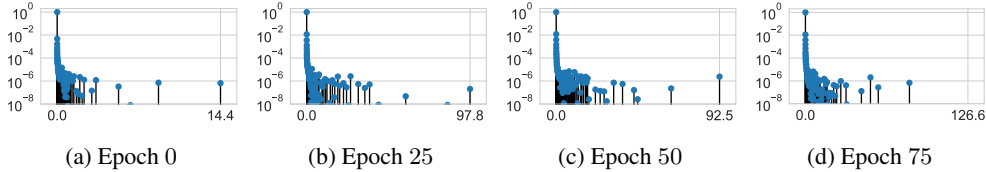


Figure 23: Generalised Gauss Newton full empirical spectrum for the PreResNet-110 on the CIFAR-100 dataset, total training 225 epochs, batch norm eval mode

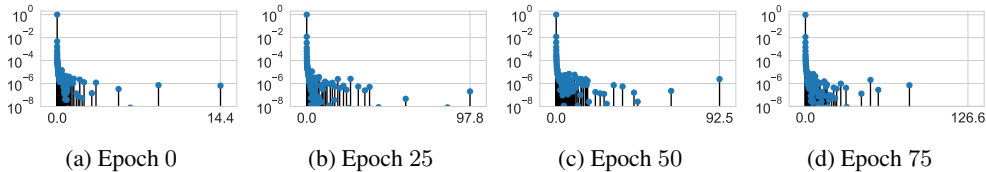


Figure 24: Generalised Gauss Newton full empirical spectrum for the PreResNet-110 on the CIFAR-100 dataset, total training 225 epochs, batch norm eval mode

Similarly to the previous section, we show in Figure 27 that even with batch normalisation in evaluation mode, the sub-sampling procedure induces extreme spectral broadening, compared to the same points in weight space with the full dataset, shown in Figure 26. Again although the results are stochastic, with large variance the trend is consistent.

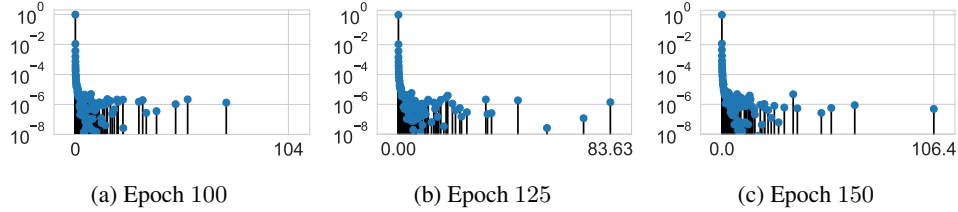


Figure 25: Generalised Gauss Newton full empirical spectrum for the PreResNet-110 on the CIFAR-100 dataset, total training 225 epochs, batch norm eval mode

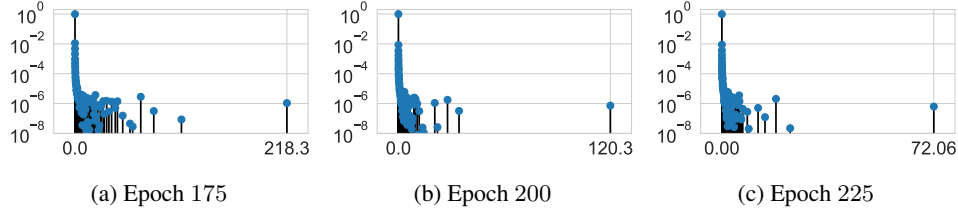


Figure 26: Generalised Gauss Newton full empirical spectrum for the PreResNet-110 on the CIFAR-100 dataset, total training 225 epochs, batch norm eval mode

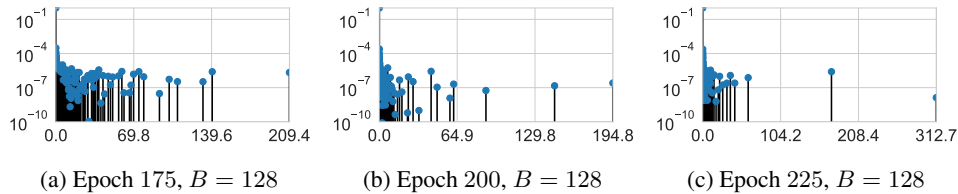


Figure 27: Generalised Gauss Newton full empirical spectrum for the PreResNet-110 on the CIFAR-100 dataset, total training 225 epochs, batch norm eval mode, $B = 128$ sub-sampled spectrum

H.2.1 Hessian - batch normalisation train mode

Similar to the Generalised Gauss Newton, the Hessian has well separated both negative and positive outliers from the spectral bulk and a large rank degeneracy, these observations are consistent throughout training.

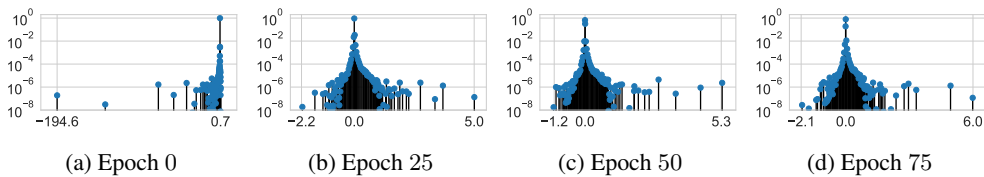


Figure 28: Hessian full empirical spectrum for the PreResNet-110 on the CIFAR-100 dataset, total training 225 epochs, batch norm train mode

Similarly at all points in training, stochastic batch Hessia are shown to be significantly broadened, we see this by comparing the full data empirical Hessian spectrum 29 compared to the Hessian at the same point in weightspace but using only a batch size of $B = 128$ in Figure 30.

H.2.2 Hessian - batch normalisation evaluation mode

Similarly at all points in training, stochastic batch Hessia in evaluation mode are shown to be significantly broadened, we see this by comparing the full data empirical Hessian spectrum 33 compared to the Hessian at the same point in weightspace but using only a batch size of $B = 128$ in Figure 34.

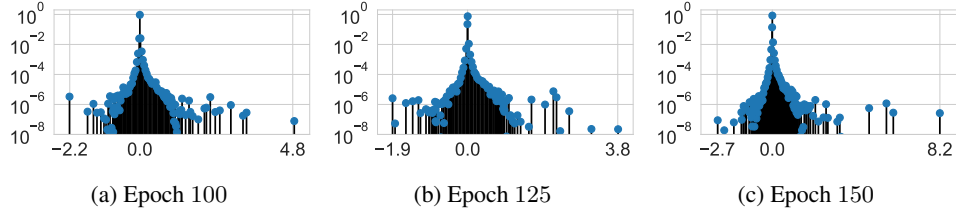


Figure 29: Hessian full empirical spectrum for the PreResNet-110 on the CIFAR-100 dataset, total training 225 epochs, batch norm train mode

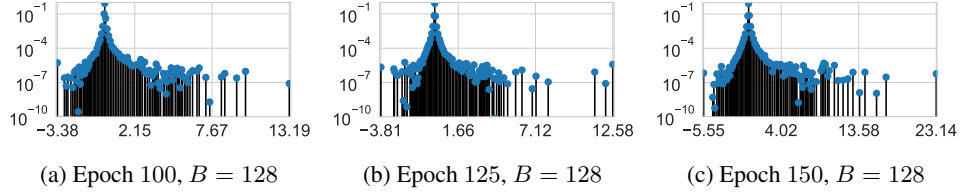


Figure 30: Hessian batch spectrum for the PreResNet-110 on the CIFAR-100 dataset, total training 225 epochs, batch norm train mode, $B = 128$

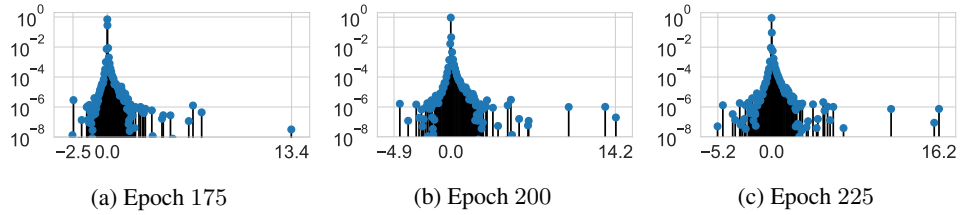


Figure 31: Hessian full empirical spectrum for the PreResNet-110 on the CIFAR-100 dataset, total training 225 epochs, batch norm train mode

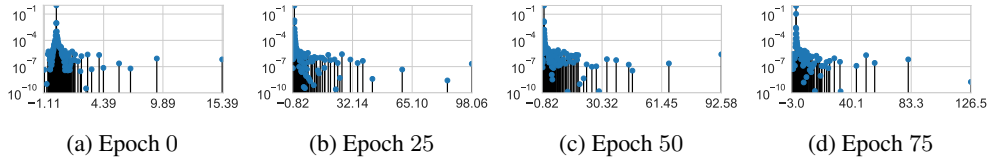


Figure 32: Hessian full empirical spectrum for the PreResNet-110 on the CIFAR-100 dataset, total training 225 epochs, batch norm evaluation mode

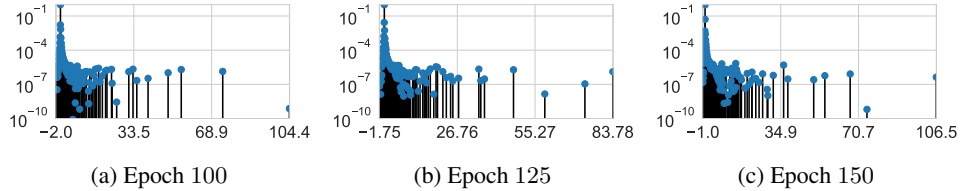


Figure 33: Hessian full empirical spectrum for the PreResNet-110 on the CIFAR-100 dataset, total training 225 epochs, batch norm evaluation mode

I Further results and datasets

I.1 VGG16

We include the full results for the VGG-16 generalised Gauss-Newton and Hessian spectra.

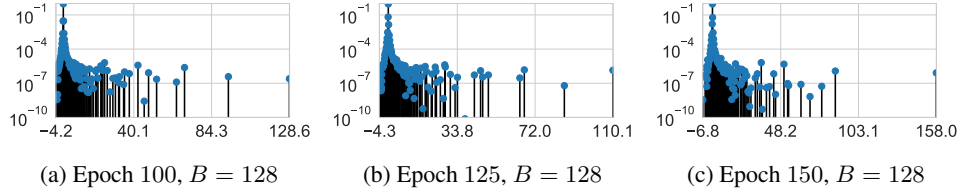


Figure 34: Hessian batch spectrum for the PreResNet-110 on the CIFAR-100 dataset, total training 225 epochs, batch norm train mode, $B = 128$

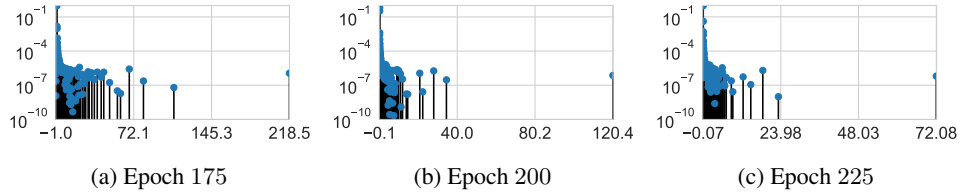


Figure 35: Hessian full empirical spectrum for the PreResNet-110 on the CIFAR-100 dataset, total training 225 epochs, batch norm evaluation mode

I.1.1 Generalised Gauss Newton

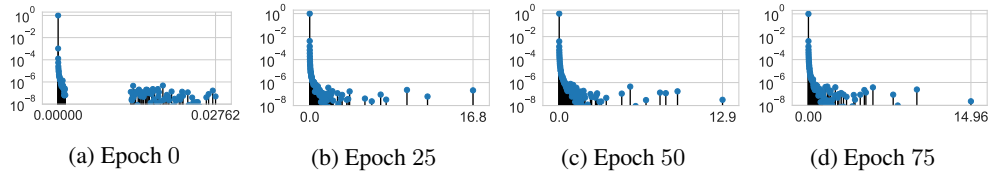


Figure 36: Generalised Gauss Newton full empirical spectrum for the VGG-16 on the CIFAR-100 dataset, total training 225 epochs, batch norm train mode

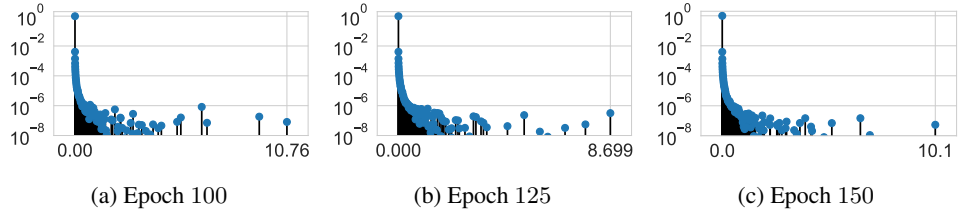


Figure 37: Generalised Gauss Newton full empirical spectrum for the VGG-16 on the CIFAR-100 dataset

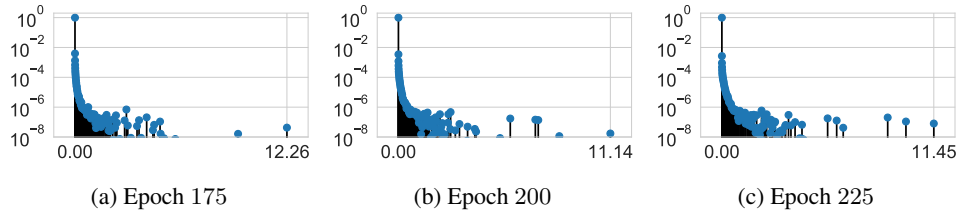


Figure 38: Generalised Gauss Newton full empirical spectrum for the VGG-16 on the CIFAR-100 dataset

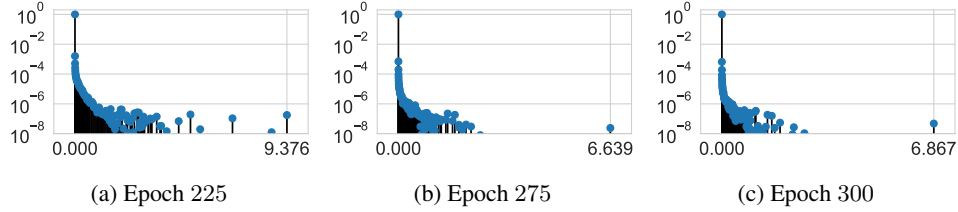


Figure 39: Generalised Gauss Newton full empirical spectrum for the VGG-16 on the CIFAR-100 dataset

I.1.2 Hessian

To showcase the visualisation for different values of m , we use $m = 30$, for the VGG-16 on the CIFAR-100 dataset. Even for a less moment matched spectrum, we note identical features in terms of large seeming rank degeneracy, a spread out bulk and large well separated outliers.

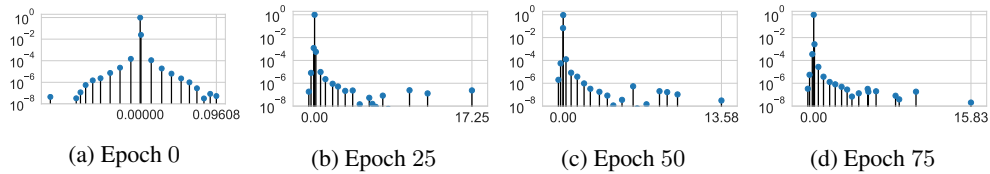


Figure 40: Hessian full empirical spectrum for the VGG-16 on the CIFAR-100 dataset, total training 225 epochs, batch norm train mode

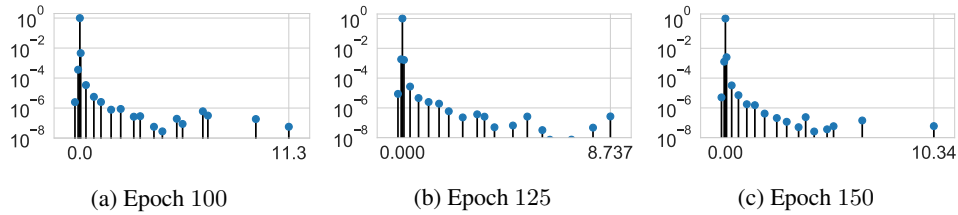


Figure 41: Hessian full empirical spectrum for the VGG-16 on the CIFAR-100 dataset

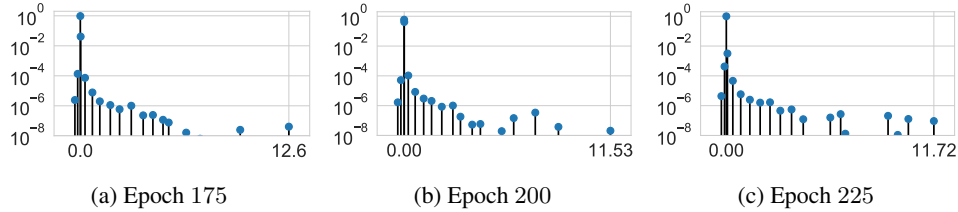


Figure 42: Hessian full empirical spectrum for the VGG-16 on the CIFAR-100 dataset

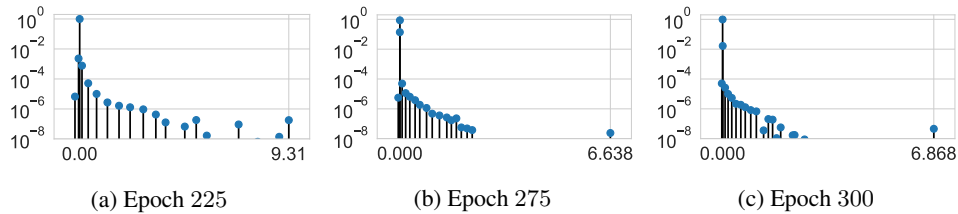


Figure 43: Hessian full empirical spectrum for the VGG-16 on the CIFAR-100 dataset

J Why Weyl is insufficient

Alternatively when evaluating the sharpness of the minimum, characterized by its extremal eigenvalues, using Weyl's bound on Hermitian matrices [70, 5],

$$\Delta\lambda_i = |\lambda'_{max} - \lambda_{max}| \leq \|H_{emp} - H_{batch}\| = \|\epsilon(w)\|, \quad (45)$$

For the L_2 norm, the typical magnitude of each element of $|\epsilon(w)_{i,j}|$ can be expected to be around $\sigma_{i,j}/\sqrt{\mathbf{b}}$. I.e $\mathbb{E}(\epsilon(w)_{i,j}^2) = \sigma_{i,j}^2/\mathbf{b}$

$$\|\epsilon(w)\|_{L_2} = \sqrt{\sum_{i,j} \epsilon(w)_{i,j}^2} \approx \sqrt{\sum_{i,j} \frac{\sigma_{i,j}^2}{\mathbf{b}}} = \frac{P}{\sqrt{\mathbf{b}}} \sqrt{\sigma^2}. \quad (46)$$

This is significantly looser a bound than Theorem 2.